An inducible amphipathic helix within the intrinsically disordered C terminus can participate in membrane curvature generation by peripherin-2/rds

Received for publication, November 15, 2016, and in revised form, March 15, 2017 Published, Papers in Press, March 21, 2017, DOI 10.1074/jbc.M116.768143

Michelle L. Milstein[‡], Victoria A. Kimler[‡], Chiranjib Ghatak[§], Alexey S. Ladokhin[§], and Andrew F. X. Goldberg[‡1]

From the [‡]Eye Research Institute, Oakland University, Rochester, Michigan 48309 and the [§]Department of Biochemistry and Molecular Biology, University of Kansas Medical Center, Kansas City, Kansas 66160-7421

Edited by Paul E. Fraser

Peripherin-2/rds is required for biogenesis of vertebrate photoreceptor outer segment organelles. Its localization at the high-curvature rim domains of outer segment disk membranes suggests that it may act to shape these structures; however, the molecular function of this protein is not yet resolved. Here, we apply biochemical, biophysical, and imaging techniques to elucidate the role(s) played by the protein's intrinsically disordered C-terminal domain and an incipient amphipathic α-helix contained within it. We investigated a deletion mutant lacking only this α-helix in stable cell lines and *Xenopus laevis* photoreceptors. We also studied a soluble form of the full-length ~7-kDa cytoplasmic C terminus in cultured cells and purified from *Escherichia coli*. The α-helical motif was not required for protein biosynthesis, tetrameric subunit assembly, tetramer polymerization, localization at disk rims, interaction with GARP2, or the generation of membrane curvature. Interestingly, however, loss of the helical motif up-regulated membrane curvature generation *in cellulo*, introducing the possibility that it may regulate this activity in photoreceptors. Furthermore, the incipient α-helix (within the purified soluble C terminus) partitioned into membranes only when its acidic residues were neutralized by protonation. This suggests that within the context of full-length peripherin-2/rds, partitioning would most likely occur at a bilayer interfacial region, potentially adjacent to the protein's transmembrane domains. In sum, this study significantly strengthens the evidence that peripherin-2/rds functions directly to shape the high-curvature rim domains of the outer segment disk and suggests that the protein's C terminus may modulate membrane curvature-generating activity present in other protein domains.

The cellular basis for vertebrate vision rests upon many hundreds of precisely sculpted and stacked membranous disks that absorb visible light and scaffold a G-protein-mediated phototransduction cascade. The regularity and precision with which these membranes are organized have fascinated cell biologists for more than half a century, and their importance for photoreceptor electrophysiological function has been recognized for several decades (1, 2). In both rod and cone photoreceptors, stacked membranous disks constitute the outer segment (OS)[2] organelles of these cells. Maintaining this complex architecture represents a constant challenge for retinal photoreceptors, because a significant amount of disk membrane in each OS is renewed on a daily basis (3). The disruption of OS membrane structure or renewal by environmental and/or genetic causes compromises photoreceptor function and can lead to progressive and debilitating retinal diseases (4, 5). An improved knowledge of normal OS structure is needed to advance understanding of how perturbations trigger pathogenic processes.

The molecular basis for the formation and maintenance of photoreceptor OS membrane architecture has begun to come into focus but is not yet well resolved (4, 6). Advancing understanding in this area will require a molecular level knowledge of how individual OS disk structures are generated and maintained. Disks are defined by high-curvature rim domains at their peripheries, which are structurally and biochemically distinct (7–9). Both rod and cone disks require rim domains; mature rod disks are distinct intracellular compartments that are fully bounded by rim, whereas most (perhaps all) cone disks retain at least some measure of edge domain and therefore maintain continuity with the OS plasma membrane (10, 11). The mechanisms that create/maintain the high-curvature rim domains are of key importance, because membrane structures with diameters of this scale (~26 nm) require shaping by active mechanisms and specialized proteins (12). The question of how disk rims are shaped is not yet answered; however, several reports indicate that peripherin-2/rds (P/rds), an integral mem-

This work was supported in whole or in part by National Institutes of Health Grants EY025291(to A. F. X. G.) and EY013246 and by the Oakland University Research Excellence Fund. The authors declare that they have no conflicts of interest with the contents of this article. The content is solely the responsibility of the authors and does not necessarily represent the official views of the National Institutes of Health.

This article contains supplemental Figs. S1–S9.

[1] To whom correspondence should be addressed: Eye Research Institute, 417 Dodge Hall, Oakland University, Rochester, MI 48309. Tel.: 248-370-2393; E-mail: goldberg@oakland.edu.

[2] The abbreviations used are: OS, outer segment; P/rds, peripherin-2/rds; AH, amphipathic helix; Endo H, endoglycosidase H; IHC, immunohistochemistry; WGA, wheat germ agglutinin; GARP, glutamic acid-rich protein; ITF, intrinsic tryptophan fluorescence; LUV, large unilamellar vesicle; POPG, 2-oleoyl-1-palmitoyl-*sn*-glycero-3-glycerol; POPC, 2-oleoyl-1-palmitoyl-*sn*-glycero-3-phosphocholine; ER, endoplasmic reticulum; ERGIC, endosomal reticulum-Golgi intermediate complex; ERC, endosomal recycling compartment; TEM, transmission electron microscopy, DOPC, 1,2-dioleoyl-*sn*-glycero-3-phosphocholine; DOPE, 1,2-dioleoyl-*sn*-glycero-3-phosphoethanolamine; DOPS, 1,2-dioleoyl-*sn*-glycero-3-phosphoserine; LSCM, laser-scanning confocal microscopy; PNGase, peptide:*N*-glycosidase; dpf, days post-fertilization; PCC, Pearson's correlation coefficient.

brane protein and member of the tetraspanin superfamily, can act to generate membrane curvature (13, 14). A potential role for P/rds in curvature generation was suggested when the protein was originally localized to disk rims (15); however, direct evidence for this hypothesis had been lacking until recently.

P/rds is essential for the elaboration of photoreceptor OS organelles (16). Although generally believed to function as a structural element, its mechanism of action is not yet well resolved (6, 17). The role of its cytoplasmic C terminus is particularly puzzling, in part because this ~7-kDa intrinsically disordered domain has virtually no measurable secondary or tertiary structure in aqueous solution (18). The P/rds C terminus is nonetheless critical for physiological function, as demonstrated by the variety of pathogenic mutations that affect it (supplemental Fig. 1). Intrinsically disordered domains can acquire structure as a function of target binding (19), and membrane mimetics can induce secondary structure in the P/rds C terminus (18, 20, 21); however, it is not known whether this domain is membrane-associated in photoreceptors.

Three possibilities have been suggested with respect to the molecular activities of this domain. First, it is documented to participate in the targeting of P/rds to the OS *in vivo* (22–24). Importantly, the region essential for targeting may overlap with that which gains structure in the presence of membrane mimetics. Second, the C-terminal domain can promote membrane-membrane fusion *in vitro*, and this activity was suggested to support OS membrane structure (20, 21). Third, one recent study shows that the P/rds C terminus can generate membrane curvature *in vitro*, and it suggests that this activity may contribute to the formation and/or stability of OS disk rims (14). Given the plasticity inherent in intrinsically disordered protein regions, it is conceivable that this domain participates in several activities.

Here, we demonstrate that *bona fide* phospholipid membranes can induce an amphipathic helix (AH) in the P/rds C-terminal domain *in vitro* and that this motif is distinct from determinants for protein biosynthesis, trafficking, and interaction with GARP2. We further demonstrate that the incipient C-terminal AH is not required for P/rds membrane curvature generation but instead acts to suppress this activity.

Results

P/rdsΔAH is properly synthesized in stably transformed HEK AD293 cells

A variety of P/rds structure/function analyses have focused on disease-linked mutations in the conserved extracellular-2 region of the protein; however, less attention has been focused on the protein's intrinsically disordered cytoplasmic C terminus, which nevertheless plays a critical role for human vision (25). Here, we generated a novel deletion mutant, P/rdsΔAH, that eliminates only the residues encoding the proposed C-terminal helical motif (amino acids 310–325; illustrated in Fig. 1) to investigate its mechanistic significance.

HEK AD293 (and COS-1) cells have proven to be valuable expression systems for the analysis of P/rds (14); however, previous studies only used transiently transfected cells, which can show large cell-to-cell variability in protein expression. For this

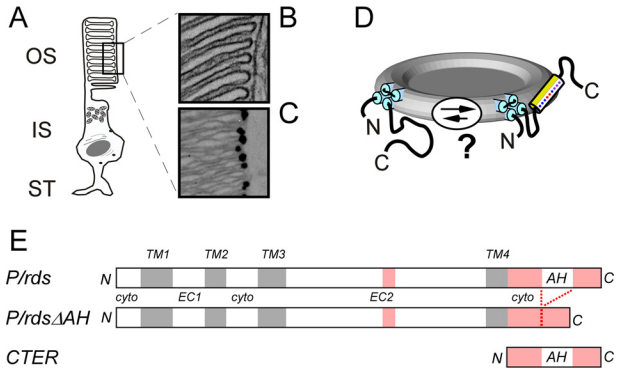

Figure 1. P/rds is a disk rim-localized integral membrane protein with an intrinsically disordered cytoplasmic C terminus of uncertain function. *A,* vertebrate rod photoreceptor OS includes a stack of internalized membranous disks that are discontinuous from and enclosed by a plasma membrane. *B,* edges of internalized OS disks are characterized by small diameter "rims," where the membranes are bent into hairpin-like high-curvature shapes. *C,* immunogold localization of P/rds to disk rims in a LR-White section of bovine retina. *D, in vitro* studies show that the P/rds C terminus is intrinsically disordered, but membrane mimetics can induce helical structure in its central region (18, 20, 21). The model presented here hypothesizes that a similar conformational change can be induced *in situ*. *E,* linear representations (drawn to scale) of the P/rds protein variants investigated in this study; they include WT P/rds, P/rdsΔAH (missing amino acids 310–325), and CTER, a soluble version of the cytoplasmic C terminus. Disordered regions are indicated in *pink*.

investigation, we also created and utilized stably expressing clonal cell lines to control for potential variability of protein expression. Stable lines were generated for the P/rdsΔAH mutant and for a WT P/rds control (described under "Experimental procedures"). We first assayed whether loss of the inducible C-terminal AH would impede protein biosynthesis. Fig. 2 shows a Western blotting analysis using the anti-P/rds monoclonal antibody MabC6 to compare P/rds variants stably expressed in HEK AD293 cell lines with native P/rds from bovine rod OS membranes. MabC6 binds an epitope at the protein's extreme C terminus and is therefore specific for fully translated P/rds (18, 26); importantly, this epitope remains intact in the P/rdsΔAH mutant. Expression of the P/rdsΔAH mutant was robust, and the protein showed a somewhat increased mobility relative to WT P/rds (Fig. 2*A*), consistent with its reduced molecular mass (~2 kDa). The P/rdsΔAH mutant was detected as several closely spaced bands, a result also commonly observed for WT P/rds. Each recombinant protein migrated more slowly than P/rds extracted from bovine rod OSs, consistent with the more extensive (and heterogeneous) glycosylation commonly associated with heterologously expressed P/rds (24, 27).

In the absence of added reducing agent, the P/rdsΔAH mutant was present in both monomeric and dimeric forms, akin to WT P/rds and P/rds from bovine rod OSs (Fig. 2*B*). The dimer/monomer ratios were similar in all three samples (~1:1). These results demonstrate that the deletion of the inducible C-terminal AH had no significant effect on the disulfide-mediated dimerization of P/rds that occurs during tetramer polymerization.

Because native P/rds is characterized by an *N*-linked carbohydrate modification that can affect its function (28), we tested the effects of glycosidases on the stably expressed recombinant proteins (Fig. 2*C*). In response to PNGase F, a mobility increase

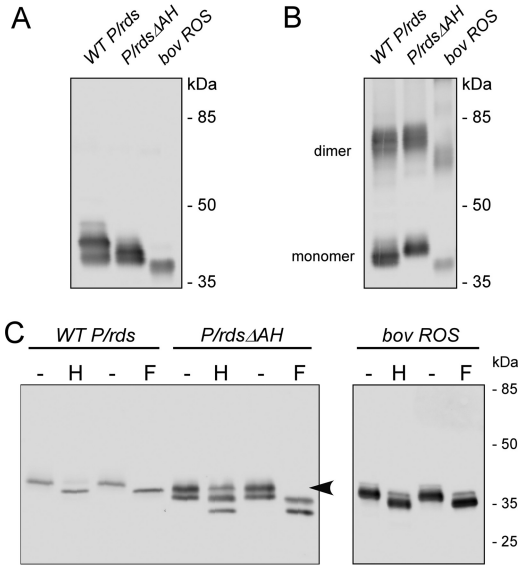

Figure 2. Deletion of the P/rds C-terminal AH does not impair protein biosynthesis or disulfide-mediated dimerization. *A* and *B,* stably expressing HEK AD293 cells were treated with *N*-ethylmaleimide to block free thiols, and Triton X-100 extracts were subjected to non-reducing (*A*) and reducing (*B*) 10% SDS-PAGE followed by Western blotting analysis with anti-P/rds monoclonal antibody MabC6. An extract from bovine rod OSs was analyzed in parallel for comparison. These data indicate that deletion of the C-terminal AH does not affect disulfide-mediated P/rds dimerization. *C,* post-translational carbohydrate modifications were analyzed using PNGase F (*F*) and Endo H (*H*) glycosidases, which cleave glycoprotein oligosaccharides. The former removes almost all types of *N*-linked glycosylation, but resistance to the latter is a signature of Golgi processing. WT P/rds expressed in cultured cells shows greater heterogeneity in glycosylation than does the native protein from rod OS membranes (27).

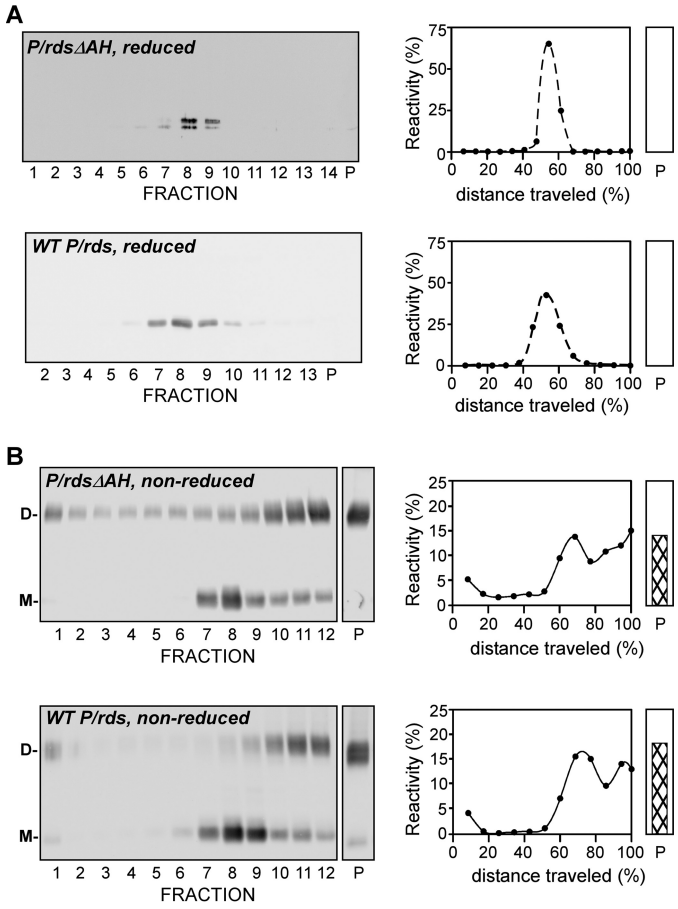

Figure 3. Deletion of the P/rds C-terminal AH does not impair tetrameric subunit assembly or disulfide-mediated tetramer polymerization. *A,* stably expressing HEK AD293 cells were treated with *N*-ethylmaleimide to block free thiols, and Triton X-100 extracts were centrifuged under reducing conditions in 5–20% (w/w) sucrose gradients. Fractionated gradients and particulate fractions (*P*) were assayed for P/rds by reducing SDS-PAGE and Western blotting analysis with MabC6. Blots were scanned and quantitated to generate the plots shown. P/rdsΔAH sediments as a single major peak, with a mobility essentially identical to that of WT P/rds and characteristic of a tetrameric stoichiometry (31). *B,* similar analyses were performed, except that centrifugations and SDS-PAGE for Western blotting analysis were performed under non-reducing conditions. In this case, P/rdsΔAH, like WT P/rds, sediments as multiple species, a characteristic of tetrameric complexes that have been integrated into polymeric chains by disulfide bonds. Both monomeric (*M*) and disulfide-linked dimeric (*D*) species are present in the non-reduced samples.

was observed for the P/rdsΔAH mutant protein, as well as for the WT P/rds protein. This finding indicates that each protein is covalently modified by the addition of an *N*-linked carbohydrate moiety. Mobility increases were also observed for each protein in response to endoglycosidase H (Endo H), although slight differences were noted in the banding patterns. Although all carbohydrate on the WT protein was Endo H-sensitive, a fraction (~30%) of the P/rdsΔAH protein appeared to be unaffected by Endo H treatment. Because Endo H resistance reflects glycan processing (and therefore protein processing by the *trans*-Golgi), this result suggests that deletion of the inducible C-terminal AH may alter secretory processing of the *N*-linked carbohydrate moiety. Altogether, these findings demonstrate that loss of the proposed C-terminal AH does not impair P/rds biosynthesis or its ability to be post-translationally modified in a manner largely similar to WT. The data also suggest that a fraction of the mutant protein may undergo differential post-translational processing.

Hydrodynamic analysis of P/rdsΔAH subunit assembly and covalent polymerization

Previous investigations have demonstrated that P/rds in native ROS membranes is characterized by several steps of self-assembly. To examine whether the inducible C-terminal AH can also contribute to protein subunit assembly and/or disulfide-mediated tetramer polymerization, we conducted a hydrodynamic analysis using a sedimentation velocity approach developed previously (26). Non-denaturing detergent lysates were extracted from HEK AD293 cells stably expressing P/rdsΔAH or WT P/rds under reducing conditions, which were then layered onto sucrose gradients and centrifuged overnight. Fig. 3*A* shows representative data from reducing Western blotting analyses of the fractionated gradients run under reducing conditions and immunoblotted with anti-P/rds MabC6. The sedimentation profile for P/rdsΔAH (Fig. 3*A*, *upper right*) was essentially identical to that of WT P/rds (Fig. 3*A*, *lower right*). Each protein was observed as a single major species, with sedimentation coefficients ($s_{20,w}$) of 5.0 ± 02 (mean ± S.D., $n = 4$) for the P/rdsΔAH mutant and 5.3 (mean, $n = 2$), for the WT; in each case these values reflect a tetrameric protein (29). No protein was found in the pellet fraction (Fig. 3*A*, *lane P*) for either variant. These observations demonstrate that P/rdsΔAH subunit assembly is unaffected by loss of its C-terminal inducible AH and that the information required to specify a tetrameric stoichiometry lies outside of this region.

When sedimentations were instead performed under non-reducing conditions, using HEK AD293 lysates extracted under disulfide-preserving conditions, P/rdsΔAH and WT P/rds each sedimented as multiple species. Fig. 3*B* shows the sedimentation profiles revealed by Western blotting analyses conducted under non-reducing conditions. In addition to a tetrameric form, each variant also showed the incorporation of tetramers into more massive forms, including significant accumulations in the pellet fraction. These larger species include octamers and higher order polymers of P/rds, formed by intermolecular disulfide bonds that link tetramers together (30). Because the sedimentation profiles of unreduced P/rdsΔAH and WT P/rds were essentially identical, it can be concluded that the C-terminal AH is not essential for the polymerization of P/rds tetramers into higher-order forms via intermolecular disulfide bonds. Altogether, the findings presented in Fig. 3 demonstrate that loss of the inducible C-terminal AH does not impair any of the known assembly processes responsible for generating normal P/rds quaternary protein structure in cultured cells. Because numerous studies demonstrate that COS-1 and HEK 293 cells are excellent model systems for P/rds subunit assembly in vertebrate photoreceptors (26, 31–35), it is likely that the P/rds quaternary structure likewise does not rely on the C-terminal inducible AH in vertebrate photoreceptors.

Trafficking of P/rdsΔAH to rod photoreceptor OSs

A previous study has highlighted the importance of P/rds tetramerization for routing the protein to its site of function in the OS organelle (36). Because subunit assembly and polymerization of the P/rdsΔAH mutant appeared normal, it was of interest to investigate its trafficking and localization in vertebrate photoreceptors. The P/rds C terminus has previously been implicated in the routing of P/rds to OSs (22, 23).

To test the importance of the AH region for P/rds targeting, we chose transgenic *Xenopus laevis* photoreceptors, a preferred system for this purpose, due to the large diameters of their OSs (37). To allow for the unique identification of the mutant protein in the context of the endogenous frog P/rds, a P/rdsΔAH minigene was constructed, based on the bovine P/rds sequence. A previous study has demonstrated that the WT bovine P/rds ortholog is properly expressed and localized in this system (38). Transgenesis was conducted by injecting IseI-digested DNA into fertilized *X. laevis* eggs, and ocular cryosections from positive F_o and F_1 tadpoles were analyzed using immunohistochemistry (IHC) and laser-scanning confocal microscopy (LSCM). Fig. 4*A* (*upper panel*) presents a double-labeling experiment, using anti-bovine P/rds polyclonal antibody PabBCT in conjunction with wheat germ agglutinin (WGA), a marker of photoreceptor OSs. The transgenic mutant protein (Fig. 4*A, red*) was present only in OSs, in a pattern consistent with labeling of disk rims. Similar results were obtained when double-labeling of the P/rdsΔAH mutant was performed with additional markers, including the Na^+K^+-ATPase (Fig. 4*A, middle panel*), which labels inner segment plasma membranes, and endogenous frog P/rds (Fig. 4*A, lower panel*), which resides solely in OS disk rim membranes. In each case, the P/rdsΔAH mutant localized solely to photoreceptor OSs in patterns expected for disk rim localization. Closer inspection of the mutant protein distribution revealed a high degree of overlap with endogenous frog P/rds. Fig. 4*B* shows representative fields from two different F_o animals; each illustrates similar labeling patterns for transgenic mutant and endogenous WT proteins. Distributions that include OS periphery labeling and longitudinal striations are characteristic of disk rim localized proteins, and they reflect the numerous incisures (infoldings) present in frog rod OS disks. Cross-sectional images (Fig. 4*B*) and movies (supplemental Figs. 2–4) from reconstructed Z-stack 3D volumes show a clear coincidence of labeling for the P/rdsΔAH mutant and WT proteins at the incisures. In sum, these data suggest that the P/rdsΔAH mutant was normally targeted and localized, so we considered the mechanism by which this occurred.

Because oligomerization is an integral feature of P/rds biosynthesis, it is possible that the P/rdsΔAH mutant protein was incorporated into endogenous WT P/rds-containing oligomers, which could then direct trafficking of the mutant protein. Such an effect could mask potential trafficking defects within the mutant protein. We therefore performed immunoprecipitation experiments to examine this possibility. Anti-frog P/rds monoclonal antibody Mab1G9 was used to immunoprecipitate endogenous frog P/rds from lysates of transgenic P/rdsΔAH *X. laevis* eyes, to test whether the (bovine) transgenic mutant protein would co-precipitate. Fig. 4*C* (*upper panel*) shows a direct comparison of lysed (*L*), unbound (*U*), and eluted (*E*) fractions, probed with Mab1G9, to assay the efficiency of the immunoprecipitation reaction. More than 62% of the endogenous frog WT P/rds immunoprecipitated under these conditions, as determined by digital densitometry. When these samples were instead probed with PabBCT (Fig. 4*C*, *lower panel*), which specifically detects the P/rdsΔAH mutant, the majority of the transgenic protein remained in the unbound fraction; only 17% co-precipitated with the endogenous WT P/rds. Because the bulk of P/rdsΔAH was not associated with endogenous P/rds, and all of the mutant protein trafficked and localized normally, it can be concluded that the C-terminal AH was not necessary for normal OS trafficking and localization to disk rim membranes.

P/rds C terminus can interact with GARP2 and does not require the AH motif to do so

P/rds is known to associate with several glutamic acid-rich proteins (GARPs); however, the molecular determinants in P/rds that mediate this interaction have not yet been identified (39). We used transient transfection of HEK AD293 cells in conjunction with immunocytochemistry to examine whether P/rds can interact with GARP2, the most prevalent GARP in photoreceptor OSs (40). Fig. 5*A* shows that GARP2 expressed in HEK AD293 cells exhibited a diffuse staining pattern, indicative of a cytoplasmic distribution. However, when co-expressed with WT P/rds in the same cell, GARP2 was recruited to the punctate distribution that is characteristic of P/rds, and its localization overlapped with that of the P/rds-containing puncta (Fig. 5*B*). This recruitment is consistent with the previously observed association between GARP2 and P/rds in bovine rod OSs (39) and indicates that other photoreceptor-specific proteins are not required for their interaction. To examine the

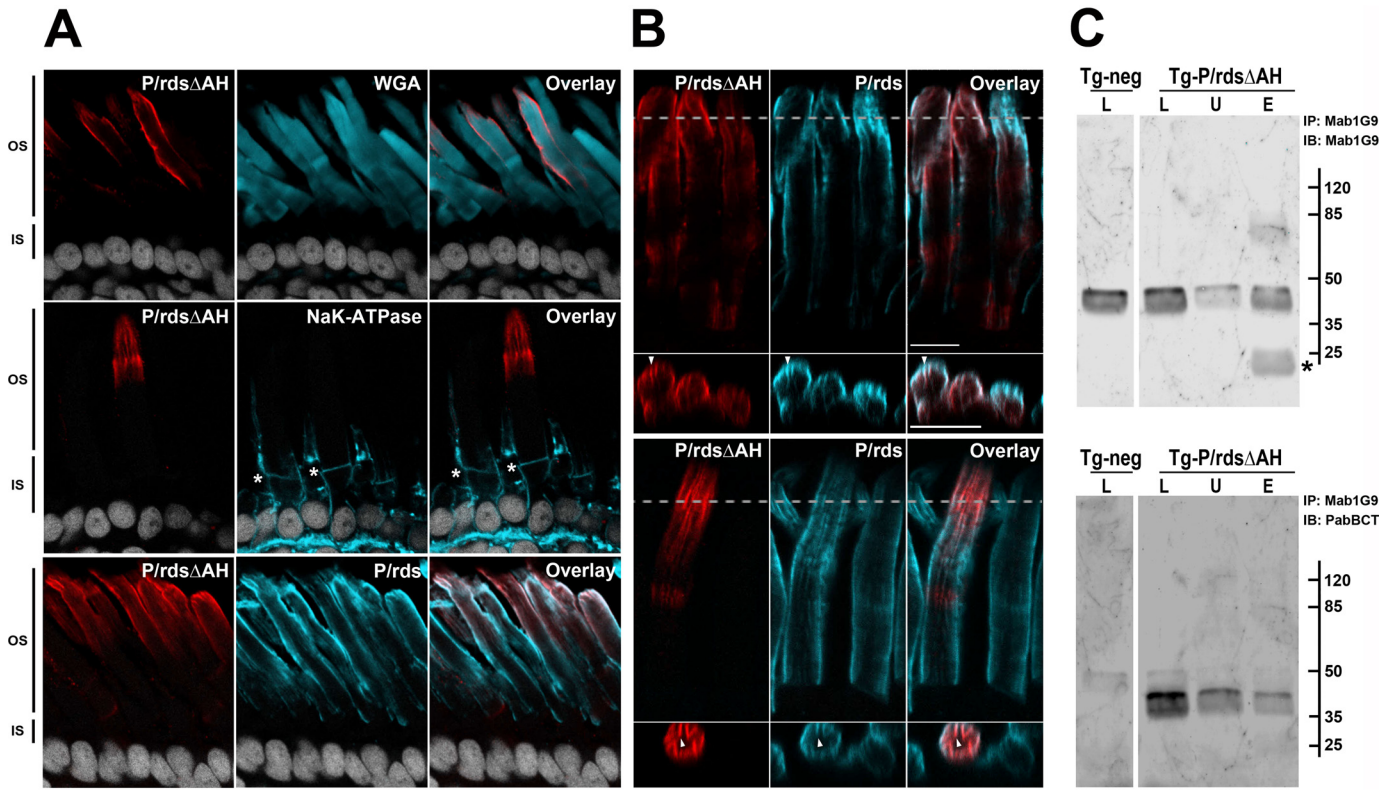

Figure 4. P/rdsΔAH is efficiently trafficked to rod photoreceptor OS disk rims in transgenic *X. laevis*. *A,* confocal images (single optical sections) of transgenic *X. laevis* photoreceptors analyzed by IHC. Ocular cryosections were double-labeled for the P/rdsΔAH mutant (*red*) and the OS marker protein WGA (*cyan, upper panels*), or the P/rdsΔAH mutant (*red*) and the inner segment marker protein Na^+,K^+-ATPase (*cyan, middle panels*), or the P/rdsΔAH mutant (*red*) and endogenous WT P/rds (*cyan, lower panels*). In each case, nuclei were counterstained with Hoechst 33342 (*white*). OS and inner segment boundaries are indicated with *asterisks* (*, *middle panels*). In every case, P/rdsΔAH localization was restricted to OSs. *B,* detailed views of IHC double labeling of P/rdsΔAH mutant (*red*) and endogenous WT P/rds (*cyan*) in transgenic photoreceptors; *upper* and *lower panels* show representative data from different cells expressing the transgenic protein. Longitudinal views (*above*) show each protein present at OS disk edges and incisures. Cross-sectional views (*below*) derived from reconstructed volumes (taken at *dotted lines*) show overlapping distribution patterns in incisures (*arrowheads*). *C,* Mab1G9 immunoprecipitation of endogenous frog P/rds from retinal lysates derived from transgenic (Tg-P/rdsΔAH) and non-transgenic (*Tg-neg*) *X. laevis*. The lysed (*L*), unbound (*U*), and eluted (*E*) fractions were assayed to measure the efficiency of the pulldown reaction for the endogenous WT P/rds (*Mab1G9*; *upper panel*) and to determine whether the transgenic P/rdsΔAH co-precipitated (*PabBCT*; *lower panel*). Although nearly all endogenous WT P/rds was immunoprecipitated (*IP*) (*upper panel*), the great majority of the mutant remained in the unbound fraction (*lower panel*) and was therefore trafficked to the OS in an independent manner. *Asterisk* (*; *upper panel*) indicates antibody light chain eluted from the Mab1G9-Sepharose beads used for immunoprecipitation. *IB*, immunoblot.

possibility that the P/rds C terminus participates in this association, GARP2 was co-expressed with a (~7-kDa) soluble version of the P/rds C-terminal domain (His_6-CTER). In co-expressing cells, GARP2 and His_6-CTER each showed diffuse and partially overlapping cytoplasmic distributions, results consistent with an interaction (Fig. 5*C*). To examine the importance of the inducible AH, we co-expressed GARP2 with the P/rdsΔAH mutant protein. Similar to WT P/rds, the AH deletion mutant effectively recruited GARP2 from a diffuse cytoplasmic distribution to a punctate localization (Fig. 5*D*). Taken together, the immunocytochemical analyses confirmed a previously reported interaction between GARP2 and P/rds, found that no other photoreceptor-specific proteins were required, and demonstrated that the region encoding the inducible C-terminal AH was not required for this interaction.

To further explore the possibility that GARP2 can interact with the P/rds C terminus in HEK AD293 cells, protein levels of co-expressing cells were assessed by Western blotting analysis. Fig. 5*E* compares the expression of His_6-CTER in HEK AD293 cells in the absence and presence of GARP2 and shows that the concentration of the P/rds C terminus is dramatically increased when GARP2 is co-expressed. Reciprocal stabilization of GARP2 by WT P/rds and by the P/rdsΔAH mutant was also observed (Fig. 5*F*); however, the magnitude of the effect was less dramatic. Taken together, these results add weight to the immunocytochemical findings and suggest that the P/rds cytoplasmic C terminus can participate in P/rds interaction with GARP2.

Bona fide phospholipid membranes induce C-terminal AH folding and partitioning

Because we found that the proposed AH region was not essential for several aspects of P/rds structure and function, we thought it prudent to re-examine the proposal that this motif can interact with and partition into phospholipid membranes. Although several studies have shown that membrane mimetics can induce a portion of the C terminus to adopt an AH structure (18, 20, 21), technical challenges have prevented an assessment of whether *bona fide* phospholipid membranes can induce a similar conformational change that includes membrane partitioning.

We first used the MPEx prediction web tool (41) to model the thermodynamics of CTER AH partitioning from a disordered state (in aqueous solution) into a helical form embedded in a

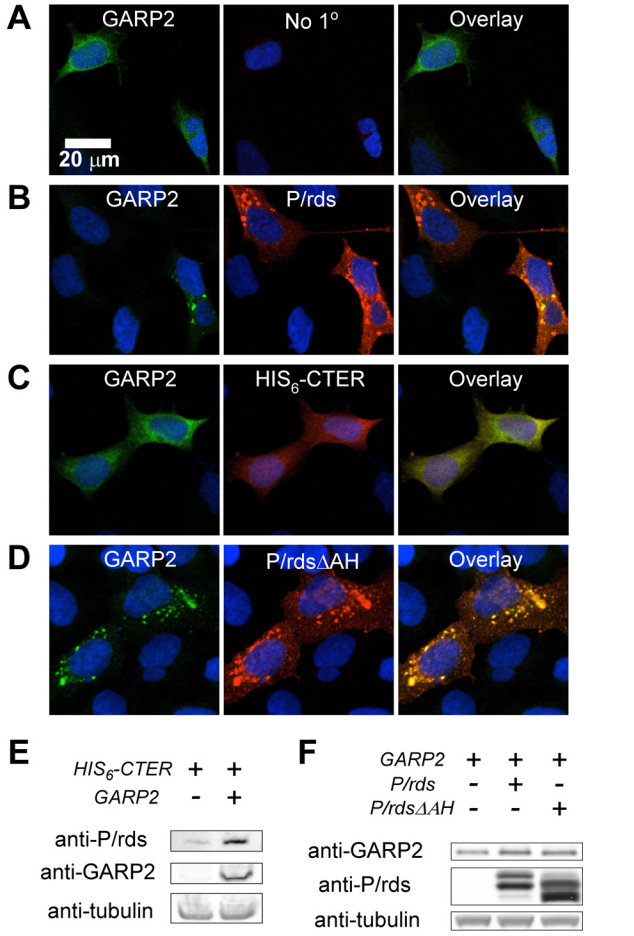

Figure 5. P/rds interaction with GARP2 does not require the AH motif. Immunocytochemical localization of GARP2 and P/rds variants in transiently transfected HEK AD293 cells. In each case, cell nuclei are stained *blue*, GARP2 reactivity appears in *green*, P/rds reactivity appears in *red*, and co-localized proteins appear *yellow*. *A,* characteristic diffuse cytoplasmic localization of GARP2 in singly transfected HEK AD293 cells. *B,* redistribution of GARP2 to small puncta occurs upon co-expression with WT P/rds. *C,* diffuse localization is retained upon co-expression with a soluble form of the P/rds C terminus, and significant co-localization is present. *D,* GARP2 is effectively recruited into puncta by P/rdsΔAH. *E,* Western blotting analysis of 6xhCTER, a soluble form of the P/rds C terminus, demonstrates robust stabilization by GARP2 co-expression in HEK AD293 cells. *F,* Western blotting analysis of GARP2 demonstrates moderate stabilization by co-expression of full-length WT P/rds or P/rdsΔAH.

membrane interface. Only weak partitioning was predicted at a neutral pH when the two glutamic acid residues present (Glu-314 and Glu-321) would be charged ($\Delta G = -2.2$ kcal/mol). In contrast, when these charges were neutralized (*i.e.* by low pH, salt-bridge formation, or pK_a perturbation) (42–44), partitioning into the membrane phase was substantially favored ($\Delta G = -6.3$ kcal/mol). Therefore, an initial analysis of CTER intrinsic tryptophan fluorescence (ITF) was conducted at a low pH (4.5). In the absence of membranes, CTER tryptophan fluorescence peaked at 355 nm, a value typical for a solvent-exposed residue (Fig. 6*A*, *bottom-most curve*). Addition of anionic large unilamellar vesicles (LUVs) with a phospholipid composition resembling that of rod OSs ("OS-like LUVs"; described in "Experimental procedures") caused a blue shift in the peak maxima and an increase in fluorescence intensity (Fig. 6*A*). A plot of the relative fluorescence intensity shows a clear and saturating dependence upon lipid concentration (Fig. 6*B*, *red symbols*) that is well fit (Fig. 6*B*, *red line*) by a simple partitioning model (described under "Experimental procedures"), which indicates a free energy of transfer (ΔG) from the aqueous phase to the membrane of −8.2 kcal/mol. Likewise, titration of CTER with *uncharged* neutral OS-like LUVs (no phosphatidylserine) also resulted in tryptophan partitioning of somewhat lesser favorability, displaying a ΔG of −7.6 kcal/mol (Fig. 6*B*, *blue symbols*). Finally, CTER partitioning into anionic 2-oleoyl-1-palmitoyl-*sn*-glycero-3-glycerol (POPG)/2-oleoyl-1-palmitoyl-*sn*-glycero-3-phosphocholine (POPC) LUVs, a standard reference system used for peptide-membrane interaction studies (described under "Experimental procedures"), was strongly favored (Fig. 6*B*, *black symbols*) and gave a ΔG of −8.4 kcal/mol. Altogether, these findings provide the first direct evidence that CTER interaction with *bona fide* membranes includes tryptophan partitioning into the bilayer hydrophobic core.

Because MPEX predictions suggested a significant pH effect on partitioning, we next performed pH titrations of CTER ITF, using OS-like LUVs (Fig. 6*C*, *red symbols*), and POPG/POPC LUVs (Fig. 6*C*, *black symbols*). The titration data demonstrate CTER tryptophan partitioning into each membrane composition was pH-dependent and could be fit by a simple two-state function. In each case, adjusting solutions to more acidic pH resulted in blue-shifted ITF peak maxima, which reflected tryptophan partitioning out of the aqueous phase and into the membrane. Fitting these data with previously described titration equations (44) (Fig. 6*C*, *solid lines*) yielded apparent pK_a values and cooperativity coefficients of 6.5 ± 0.3 (n = 1.0 ± 0.6) for the OS-like LUVs and 5.8 ± 0.1 (n = 1.4 ± 0.1) for the POPG/POPC LUVs.

We next applied far UV-CD spectroscopy, which reports on protein secondary structure content, to assess whether phospholipid membranes can affect CTER structure. Fig. 6*D* demonstrates that at pH 4.5 in the presence of POPG/POPG LUVs, CTER displays prominent negative ellipticity bands at 208 and 222 nm (*green line*); these bands indicate significant α-helical content. When shifted to neutral pH (8.0), the polypeptide instead gave a strong negative ellipticity band at ~200 nm (Fig. 6*D*, *red line*), revealing a loss of helical and an increase in random coil content. A similar spectrum was generated by CTER at pH 4.5 in the absence of LUVs (Fig. 6*D*, *black line*). These results confirm the ITF findings above (that CTER tryptophan partitioning *in vitro* is pH-dependent), and they support the hypothesis that biological membranes can induce the central portion of the intrinsically disordered CTER domain to form an AH in a coupled partitioning-folding reaction. Moreover, these data indicate that when the remainder of the P/rds protein is absent, the interaction of CTER with membranes is favored by acidic pH.

Localization of heterologously expressed P/rdsΔAH in stably transformed HEK AD293 cells

Because the inducible AH was not required for normal protein biosynthesis, interaction with GARP2, or for OS localization in photoreceptors, we further investigated its role in stably transformed cultured cells. Previous studies have shown that WT P/rds expressed in transiently transfected HEK AD293 cells is mainly localized in small puncta (often present in an

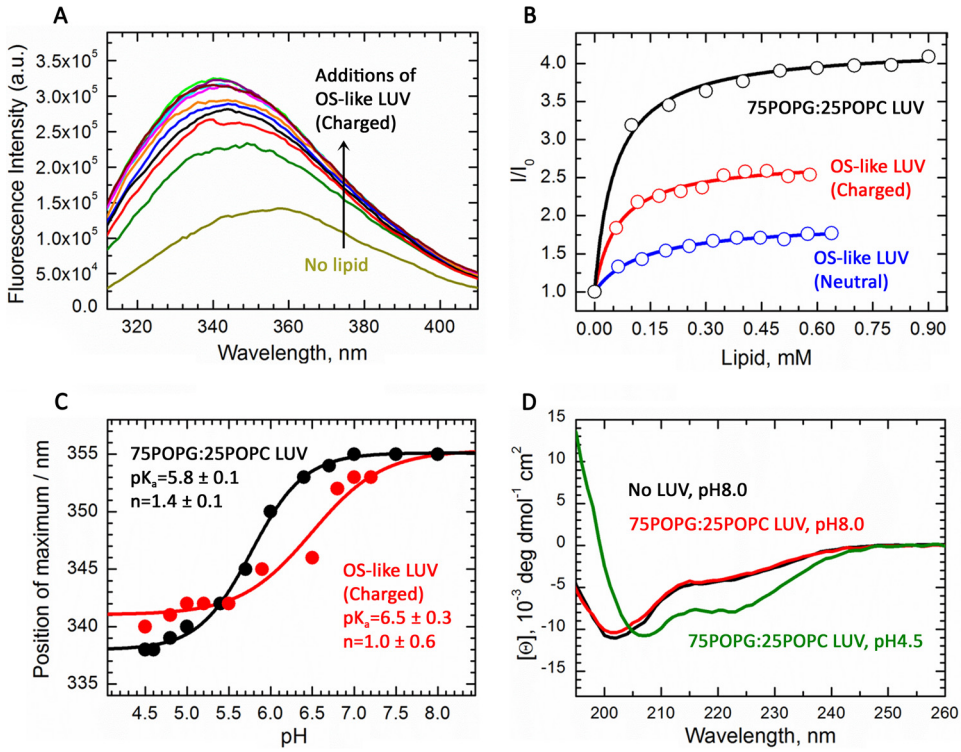

Figure 6. *Bona fide* phospholipid membranes induce partitioning-folding of an AH in the intrinsically disordered P/rds C terminus. *A,* intrinsic tryptophan fluorescence spectrum of CTER in the absence (*light green/yellow line*) or presence of charged OS-like LUVs at pH 4.5 (*various colors*). Lipid concentrations correspond to those indicated by the *red titration curve* in *B*. Increases in membrane concentration cause blue-shifts and increased fluorescence intensities, consistent with the decrease in polarity of tryptophan environment upon membrane insertion. *B,* change of fluorescence intensity is plotted as a function of lipid concentration for OS-like LUVs (*red circles*), uncharged OS-like LUVs (*blue circles*), and POPG/POPC LUVs (*black circles*). Each titration generates ITF signal changes that are well fit by simple binding equations (described under "Results"; *solid lines*). The results demonstrate that the free energy of transfer of CTER into OS-like LUVs ($\Delta G = -8.2$ kcal/mol) is somewhat more favorable than of uncharged OS-like LUVs ($\Delta G = -7.6$ kcal/mol); results for POPG/POPC LUVs ($\Delta G = -8.4$ kcal/mol) are shown for comparison with a previously documented reference composition used for peptide-membrane partitioning studies. *C,* partitioning of the CTER AH into membranes is pH-dependent. The change of peak fluorescence intensity is plotted as a function of pH for OS-like LUVs (*red circles*) and POPG/POPC LUVs (*black circles*). The data are fit (*solid lines*) to a titration equation (44) using the following parameters: $pK_a = 6.5 \pm 0.3$ ($n = 1.0 \pm 0.6$); $pK_a = 5.8 \pm 0.1$ ($n = 1.4 \pm 0.1$) for the OS-like and POPG/POPC LUVs, respectively. *D,* circular dichroism spectra of CTER in the presence of 1 mM POPG/POPC LUVs at pH 8.0 (*red line*) and pH 4.5 (*green line*), or absence of LUVs at pH 8.0 (*black line*). The induction of two negative ellipticity bands centered at 222 and 208 nm by LUVs at low pH indicate a conformational change from random coil to α-helix.

irregular perinuclear density), and relatively little protein is detected at the plasma membrane (14). To assess the impact that deletion of the C-terminal AH had on P/rds distribution in HEK AD293 cell lines, we performed double-labeling immunocytochemical analyses, using a series of membranous organelle markers in conjunction with LSCM. Fig. 7*A* shows co-localization of the WT P/rds protein with markers for the endoplasmic reticulum (ER; KDEL), the ER-Golgi intermediate complex (ERGIC; p58), the Golgi (giantin), and the endosomal recycling compartment (ERC; Rab11). The vast majority of the stably expressed WT protein was distributed in distinct intracellular puncta, a result similar to that previously reported for transiently transfected WT P/rds in HEK AD293 cells (14). Puncta distributions in different cells varied, whereas some were relatively broad (Fig. 7*A, panels a* and *g*), most showed perinuclear clustering (Fig. 7*A, panels d* and *j*). In no instance did the P/rds-containing puncta significantly co-localize with any of the organelle markers (Fig. 7*A, panels c, f, i,* and *l*); this outcome is very similar to that previously observed for P/rds expressed in transiently transfected HEK AD293 cells (14). Interestingly, labeling of the P/rdsΔAH mutant was noticeably different from WT; significantly fewer small puncta were generated, and large, often oblate, inclusions were typically present in these cells (Fig. 7*B*, *panels a, d, g,* and *j*). Like the WT, the mutant protein was largely localized in intracellular structures, rather than at the plasma membrane. Double labeling showed that these structures were largely distinct from the intracellular membranous organelles surveyed, including the nucleus, ER, ERGIC, Golgi, and ERC (see supplemental Figs. 5–8 for 3D volumes). We did, however, note that the borders of the P/rdsΔAH inclusions sometimes showed the presence of significant anti-KDEL reactivity. Altogether, these results demonstrate that loss of the P/rds C-terminal AH results in the accumulation of P/rds in discrete membranous inclusions. Because WT P/rds in small puncta was reported to induce tubulovesicular networks of small-diameter membranes in cultured cells (14), we used transmission electron microscopy (TEM) to examine the ultrastructure of the larger inclusions induced by P/rdsΔAH expression. TEM visualization is a well established assay for membrane curvature in cultured cells (45).

P/rds does not require its C-terminal AH to effectively generate membrane curvature

Fig. 8*A* illustrates a typical inclusion found in an HEK AD293 cell line stably expressing the P/rdsΔAH mutant (*arrowheads*). This structure displays a circular or oblate shape, with dimen-

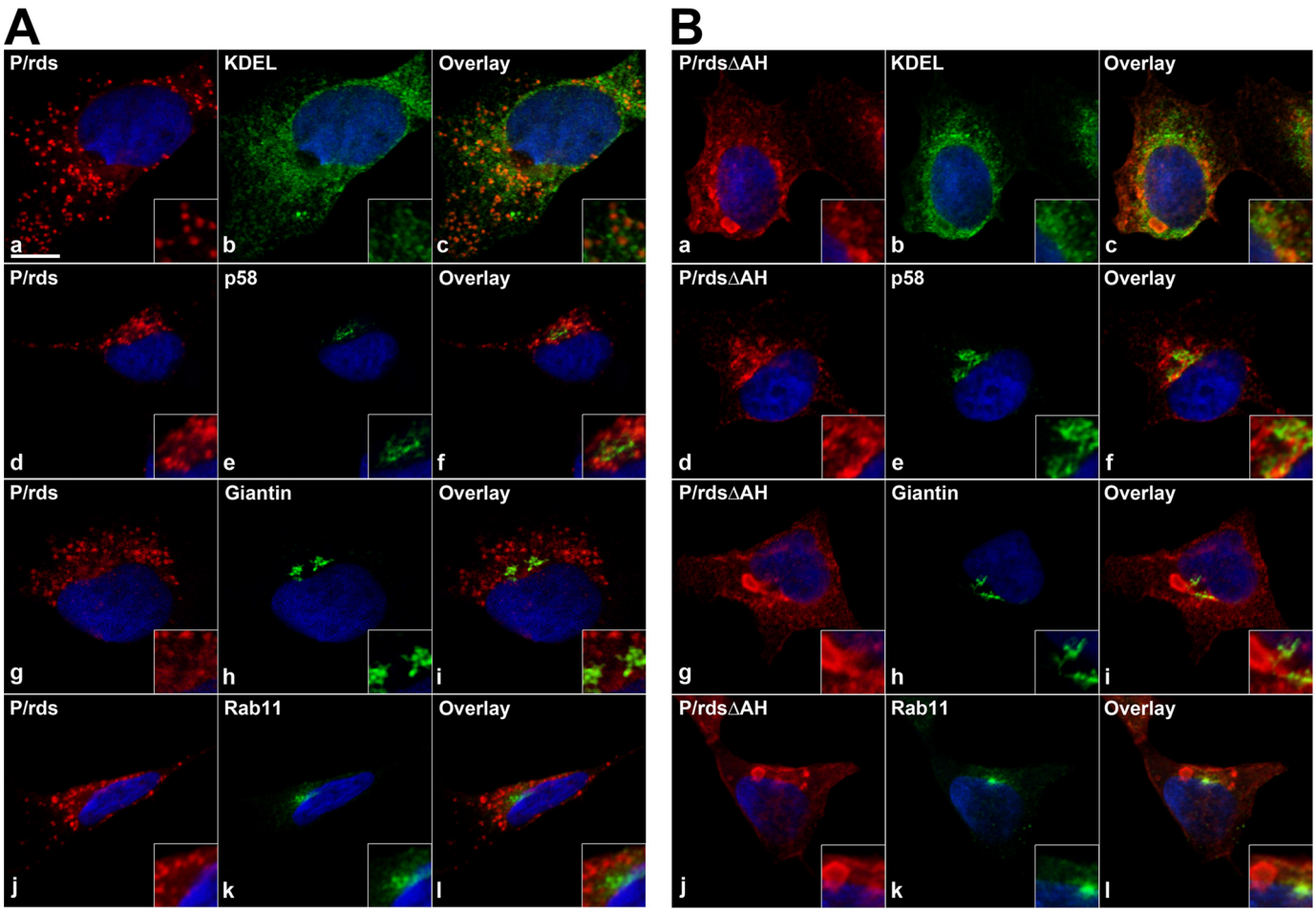

Figure 7. P/rdsΔAH forms inclusions that appear largely distinct from secretory pathway organelles in cultured cells. LSCM analysis of HEK AD293 cells stably expressing either WT P/rds (*A*) or mutant P/rdsΔAH (*B*) were double-labeled for indirect immunofluorescence with reagents directed against P/rds (*red*) and a marker (*green*) for ER (KDEL), ERGIC (p58), Golgi (giantin), or ERC (Rab11) organelles. Nuclei are counterstained with Hoechst 33342 (*blue*). Single optical sections from representative cells with moderate protein expression levels are shown. The majority of each protein was distributed in discrete puncta (WT) or large inclusions (P/rdsΔAH), which were distinct from the membranous organelles surveyed. No significant co-localization was observed between WT P/rds or P/rdsΔAH and any of the membranous compartments. Co-localization was quantified by Pearson's correlation coefficient (PCC) using the Nikon Elements software. For WT P/rds, the PCCs were as follows: KDEL, 0.61; p58, 0.47; giantin, 0.35; Rab11, 0.53. For mutant P/rdsΔAH, the PCCs were as follows: KDEL, 0.65; p58, 0.44; giantin, 0.40; Rab11, 0.42. 3D volume views reconstructed from Z-section stacks (including double labelings against KDEL and giantin) are provided as supplemental Figs. 5–8. *Scale bar*, 10 μm.

sions (~2.5 μm diameter) that are comparable with the inclusions observed by LSCM (*cf.* Fig. 7*B, panel j*). Inclusions were present in 20–50% of all cells examined by TEM, a proportion comparable with that observed by LSCM (roughly 50–75%), given that TEM thin sections sample a relatively small fraction of a given cell. No such inclusions were observed in a negative control line stably expressing Rom-1 ($n = 20$). A higher magnification view (Fig. 8*B*) reveals that the inclusion was densely packed with membranes. We previously described the appearance of "a tubulovesicular network of membranes" induced by WT P/rds, to describe a seemingly interconnected system of membranous tubules and vesicles (14). Our new results demonstrate that the P/rdsΔAH mutant (like WT P/rds) can generate small-diameter tubules; however, the mutant-induced structures were far more regular and extensive and can therefore be confidently interpreted as a network of interconnected tubules (of more extended lengths and relatively constant-diameters), often joined by three-way junctions (Fig. 8*B*, *arrowheads*). Higher magnification views (Fig. 8*C*) allowed close examination of individual tubules in both longitudinal and end-on (*arrow*) orientations and revealed their trilaminar membrane structure. Morphometric analysis (Fig. 8*D*) found an average tubule diameter of 25.1 ± 3.7 nm (mean ± S.D., $n = 299$), a value comparable with that of photoreceptor OS disk rims (~20–26 nm, dependent on species and investigator).

Remarkably, we found that some tubules imaged at higher magnifications displayed regular and distinct striations along their longitudinal axes (Fig. 8*E*). Striations possessed a periodicity of roughly 5.5 nm in the high-curvature tubules we analyzed (five repeats per 27-nm tubule). Because striations were relatively common, but were not present in every tubule, it seems likely that only the subset of tubules that were both aligned with the plane of the section, and were lying largely within it, displayed these features. This interpretation was confirmed by the appearance of tubules sectioned in transverse orientations (Fig. 8*E*, *inset*). In these cases, a pattern of ~12 units was observed in tubules of similar dimensions. Interestingly, the diameter of P/rds-Rom-1 tetramers isolated from rod OS membranes was estimated at ~6 nm (13), suggesting that

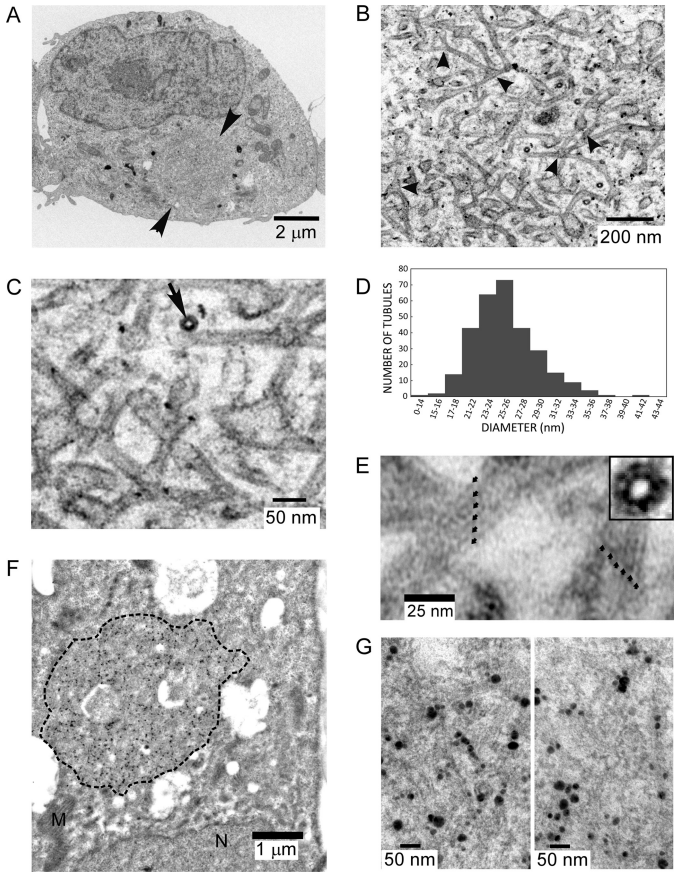

Figure 8. P/rdsΔAH displays robust membrane curvature-generating activity. *A,* transmission electron micrograph of a post-stained HEK AD293 cell stably expressing P/rdsΔAH shows a large inclusion (*arrowheads*), possessing dimensions similar to those documented by immunocytochemistry (Fig. 7*B*). *B,* higher magnification view of the inclusion, illustrating the dense network of tubulovesicular membranes within it; several three-way junctions are evident (*arrowheads*). *C,* higher magnification view from the same inclusion illustrates the trilaminar structure of the membranes, a high-curvature tubule sectioned in a transverse orientation (*arrow*), and several junctions. *D, histogram* illustrating diameters of tubules generated by P/rdsΔAH expression. *E,* tubules imaged at higher magnifications display regular substructure. Two tubules (~26-27- nm diameters) showing striations along their longitudinal axes with a repeat of roughly 5.5 nm (*small arrows*). *Inset,* a transverse section shows a similar periodicity. *F,* transmission electron micrograph of a HEK AD293 cell stably expressing P/rdsΔAH, labeled with anti-P/rds monoclonal antibody Mab2B6 and anti-mouse-IgG nanogold followed by silver enhancement. The large inclusion (*dotted perimeter*) shows robust labeling. *G,* higher magnification views of immunogold inclusion labeling showing the presence of P/rdsΔAH in the tubulovesicular membranes. The reduced ultrastructural preservation (*i.e. versus C*) is typical for immunogold labeling experiments, because milder fixation conditions are needed to retain antigenicity.

the striations documented here represent regularly arrayed P/rds-containing tetramers.

To further understand the relationship between P/rdsΔAH expression and tubulovesicular membrane induction, we performed immunogold labeling to localize the mutant protein at the ultrastructural level. Labeling with anti-P/rds monoclonal antibody Mab2B6 generated highly specific patterns of immunogold labeling in a subset (~25%) of cells, a fraction comparable with the frequency of tubulovesicular membrane inclusions observed by TEM and by IHC. Moreover, labeling distributions within individual cells were confined to circular or oblate profiles with dimensions comparable with the tubulovesicular membrane inclusions (Fig. 8*F*). Essentially, all immunogold labeling could be inhibited by pre-incubation of the primary antibody with a 16-amino acid synthetic peptide corresponding to the Mab2B6 epitope. Although the mild fixation conditions required to preserve antigenicity somewhat reduced ultrastructural preservation, tubulovesicular membrane features were retained and were discernible at higher magnifications. Close inspection of the data revealed many instances of P/rdsΔAH reactivity associated with the high-curvature tubules (Fig. 8*G*). Taken together, the conventional and immunogold TEM analyses indicate that deletion of the AH from the P/rds C terminus does not prevent this protein from generating high-curvature membranes *in cellulo*.

Given that P/rds could generate membrane curvature in the absence of its C-terminal AH, we were motivated to compare P/rdsΔAH activity to that of the WT protein. Fig. 9*A* illustrates typical inclusions produced by each protein. The tubulovesicular membrane inclusions in P/rdsΔAH-expressing cells appeared to be more frequent, larger, and more highly organized than those previously documented in the WT P/rds-expressing cells (14), so we suspected that the deletion mutant possessed enhanced activity. Three noteworthy differences were apparent. First, the frequency of inclusions was far greater in P/rdsΔAH (20–50%) *versus* WT P/rds (<3%)-expressing cells. Second, the extent of the inclusions (measured as area) generated by P/rdsΔAH was at least 100-fold greater (~1 μm^2/cell) than WT P/rds (<0.01 μm^2/cell). Third, the membranes comprising the inclusions of P/rdsΔAH-expressing cells were more organized and uniform than those of WT-expressing cells. Whereas P/rdsΔAH expression routinely generated quite long high-curvature tubules of relatively consistent diameters, such structures were almost never observed in WT P/rds-expressing cells. Altogether, these findings suggested that the deletion mutant possessed enhanced membrane curvature-generating activity.

Because the P/rdsΔAH cell lines analyzed contained ~2-fold greater levels of P/rds protein than did the WT P/rds lines, we considered the possibility that this difference contributed to the differences in membrane curvature generation. Despite significant efforts, it was not possible to obtain stable lines with more closely matched protein content, so we employed a co-expression approach to compare the activities of P/rdsΔAH and WT P/rds. We reasoned that if WT P/rds activity was comparable to (or greater than) that of P/rdsΔAH, then co-expression of WT P/rds would maintain (or enhance) P/rdsΔAH curvature generation. In contrast, however, if WT P/rds activity was reduced relative to that of P/rdsΔAH, then its co-expression would inhibit P/rdsΔAH activity. Fig. 9, *B* and *C*, shows the results of transiently transfecting stably expressing P/rdsΔAH cells with WT P/rds (*right panels*) or expression vector alone (*left panels*). Remarkably, co-expression of WT P/rds in the P/rdsΔAH stable line significantly reduced the frequency, extent, and organization of tubulovesicular inclusions in the P/rdsΔAH-expressing cells, relative to transfection with empty expression vector. Co-expression of WT P/rds raised total P/rds content by ~1.5-fold and reduced inclusion frequency (proportion of cells displaying at least one tubulovesicular inclusion) from 35 ± 13% (mean ± S.D., $n = 3$) to 17 ± 12% (mean ± S.D., $n = 3$). It reduced inclusion extent (area covered per cell) from 2.8 ± 1.4

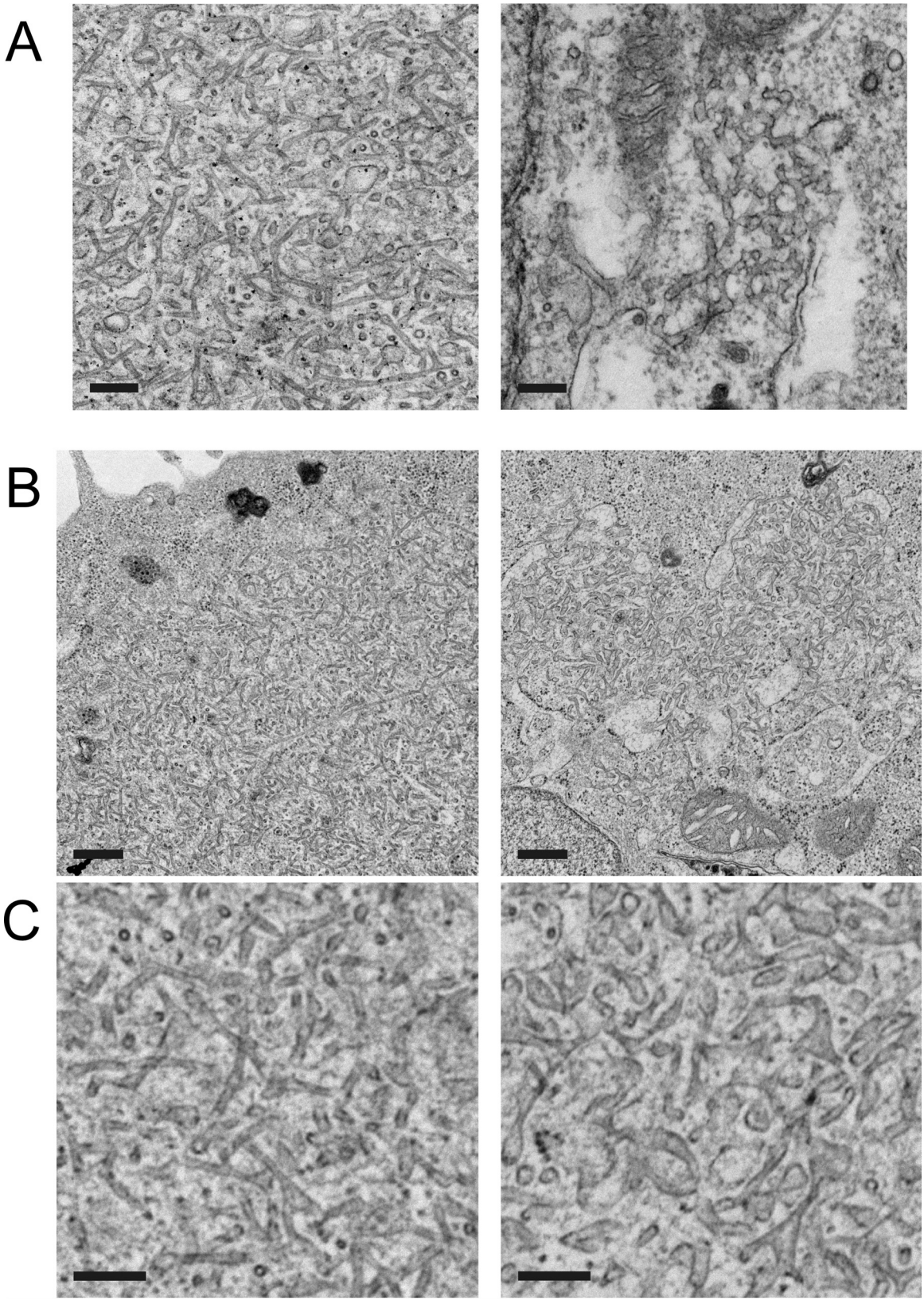

Figure 9. AH deletion enhances the extent and organization of high-curvature membrane tubules. *A,* transmission electron micrographs of tubulovesicular networks in HEK AD293 cells stably expressing P/rdsΔAH (*left*) or WT P/rds (*right*). *Scale bars,* 200 nm. *B,* transmission electron micrographs of HEK AD293 cells stably expressing P/rdsΔAH that were transfected with empty vector (*left*) or WT P/rds (*right*). Reduced extent and organization of tubulovesicular networks were seen when WT P/rds was co-expressed. *Scale bars,* 500 nm. *C,* higher magnification views from fields selected from the images presented in *B* above. Cells stably expressing P/rdsΔAH were transfected with empty vector (*left*) or WT P/rds (*right*). *Scale bars,* 200 nm.

μm/cell (mean ± S.D., $n = 3$) to 1.0 ± 0.4 μm/cell (mean ± S.D., $n = 3$). A reduction in tubulovesicular inclusion organization was apparent by visual inspection; tubules were of lower curvature (larger diameter) and more variable in shape (Fig. 9*C*; *right versus left panel*). Taken together, our findings indicate that the membrane curvature-generating activity of the P/rdsΔAH deletion mutant is enhanced relative to that of WT P/rds.

Discussion

Several animal models and a wealth of human molecular genetic data demonstrate the fundamental importance of P/rds for rod and cone photoreceptor function and viability (16, 17, 25). P/rds-associated retinal degenerations are characterized by extensive heterogeneity; however, the molecular basis for this diversity is not well understood, and this limits the ability of clinicians to counsel patients and manage disease. An improved understanding of protein function is required to resolve the molecular logic underlying P/rds genotype-phenotype relationships. This report investigates the significance of the protein's cytoplasmic C terminus, a structurally plastic and functionally essential domain, for which multiple activities have been proposed. We demonstrate that an inducible AH in the P/rds C-terminal domain is not required for membrane curvature generation *in cellulo* and that deletion of this feature up-regulates this activity. These findings suggest the possibility that the P/rds C-terminal domain may likewise act to regulate P/rds function in vertebrate photoreceptors.

This study was motivated in part by our recent report that full-length P/rds can generate membrane curvature *in cellulo* and that a soluble version of the P/rds cytoplasmic C terminus can generate membrane curvature *in vitro* (14). We proposed that membrane curvature generation by P/rds provides a molecular basis for rationalizing the energetically unfavorable small diameters of OS disk rim membranes. Although the induction of membrane curvature by proteins is not yet well understood generally, AH partitioning into membranes ("wedging") has emerged as a commonly proposed mechanism (46). Because membrane mimetics can induce an AH within the P/rds C-terminal domain (18, 20, 21), and a synthetic peptide corresponding to this region induces membrane curvature *in vitro* (14), we hypothesized that this motif might promote membrane curvature generation by full-length P/rds.

Targeted deletion of the residues encoding the P/rds C-terminal AH did not prevent expression, post-translational modification, tetrameric subunit assembly, or disulfide-mediated polymerization of the mutant protein. These observations are consistent with the intrinsically disordered nature of the C terminus (18) and with previous observations that insertion and missense mutations in this domain do not significantly affect these properties (47, 48). Loss of the C-terminal AH did slightly affect protein glycosylation. Whereas WT P/rds was fully Endo H-sensitive, a minor and variable fraction of the P/rdsΔAH mutant was Endo H-resistant. This suggests that a subpopulation of the mutant protein was processed by the *trans*-Golgi, where the enzyme that confers Endo H resistance (α-mannosidase II) resides. This result is consistent with the previous observations that full or partial removal of the inducible AH can result in acquisition of Endo H-resistant carbohydrate (24).

We found little evidence that targeting or localization in transgenic photoreceptors was affected by the P/rdsΔAH mutation. This was a somewhat surprising outcome, because previous investigations have documented that OS targeting and rim localization signals are present in the P/rds C terminus. Efficient OS targeting of GFP fusion proteins in transgenic *X. laevis* photoreceptors requires only a short sequence (10 amino acids) located downstream of the inducible AH (23); however, OS targeting that includes enrichment at disk rims requires additional upstream sequence (22). In this investigation, the vast majority of P/rdsΔAH-expressing photoreceptors correctly trafficked and targeted the mutant protein to OS disk rims. We did encounter rare examples of protein mislocalization to inner segments, but these constituted a minor fraction of the expressing cells (<5%). Because immunoprecipitation evidence showed that the bulk of the mutant protein trafficked independently of endogenous P/rds, our results indicate that the region encoding the AH is largely autonomous, both from the previously identified OS trafficking signal located downstream and from a yet-to-be defined upstream rim localization signal (22, 23). This conclusion is consistent with a previous report that found no effect of missense mutations within the AH on P/rds targeting in *Xenopus* rods (47).

Results reported here demonstrate that P/rds can associate with GARP2 and does not require its AH-encoding region, or other photoreceptor-specific proteins, to do so. Given that our data implicate the P/rds C terminus in this association, they suggest a model in which one or more of the intrinsically disordered regions flanking the membrane-inducible AH bind(s) to GARP2 (and potentially other GARPs). Although the molecular roles of P/rds-GARP interactions are not fully understood, current information suggests that they are important for the stability of OS membrane architecture (38, 39, 49, 50). Interestingly, GARPs, like the P/rds C terminus, are largely intrinsically disordered (51), and studies are needed to determine whether P/rds-GARP2 association includes mutually induced folding.

Previous investigations have used membrane mimetics to suggest that a C-terminal α-helix can partition into membranes (18, 20, 21, 52); however, direct evidence that *bona fide* membranes can induce such a structure is lacking, because the large dimensions of kinetically stable membrane vesicles interfere with many biophysical approaches. We have addressed this knowledge gap by performing ITF and CD studies under conditions that eliminate the light-scattering artifacts produced by LUVs (53, 54), and we found that *bona fide* phospholipid membranes can indeed promote folding/partitioning of a C-terminal AH. Interestingly, significant partitioning of the isolated polypeptide *in vitro* was only observed in a pH range (<6.0) below that (7.4) documented for the OS cytoplasm (55). This is consistent with theoretical MPEx predictions that protonation of the two glutamic acid residues present in the induced helical motif can affect partitioning. The pK_a values of such residues are environment-sensitive and predicted to be affected both by the lipid bilayer surface and by proteins embedded within it (42–44). Therefore, the current results suggest that if AH partitioning occurs within the context of full-length P/rds *in vivo*, it

likely does so at a lipid bilayer interfacial region, potentially involving the protein's transmembrane domains.

To test the idea that the AH motif may promote membrane curvature generation, we examined how its loss affected the membranes in which it was localized, in stably expressing cultured cells. Like WT P/rds, P/rdsΔAH was largely localized to intracellular membranes that were contained within discrete inclusions. In contrast to WT P/rds, which was localized in numerous small puncta, the mutant was concentrated in one (or a few) very large inclusion(s) per cell. Immunocytochemical analyses showed that these structures were largely distinct from intracellular membranous organelles. Interestingly, however, these inclusions contained a distinctive network of high-curvature interconnected tubules reminiscent of the tubular ER (56), and we therefore think it likely that the inclusions were ER-derived. The lack of significant anti-KDEL labeling of these inclusions was potentially due to the small diameters of their tubules, because tubule constriction is well documented to exclude luminal proteins (45, 57). Consistent with this interpretation, we also found low but significant levels of reticulon 4a, an ER tubule-shaping protein (58), associated with P/rdsΔAH-containing inclusions (supplemental Fig. 9).

The tubulovesicular inclusions produced by P/rdsΔAH were unexpectedly more frequent, larger, and more highly organized than those generated by WT P/rds. Individual tubules shaped by mutant expression possessed average diameters of ~25 nm, a value significantly smaller than the ~50-nm diameters of normal tubular ER (56), and also smaller than the ~35-nm diameters produced by WT P/rds (14). We therefore conclude that the C-terminal AH motif is not essential for membrane curvature generation by P/rds in cultured cells. This finding argues against our previous model that AH partitioning (wedging) drives P/rds generation of membrane curvature. It also counters the popular hypothesis that wedging is a mechanistically necessary aspect of membrane bending. Our finding is consistent with several recent reports, which find little or no contribution of AH wedging for endophilin (a prototypical curvature-generating protein) membrane-bending activity (59, 60). We previously demonstrated that the isolated P/rds C-terminal domain (and a peptide mimetic of the inducible amphipathic helix contained within it) can each generate membrane curvature *in vitro* (14). The current finding that this motif is not required for membrane curvature generation may therefore reflect the unique lipid composition of OS disks, an *in vivo* function for curvature sensing (*versus* curvature generation), or a non-physiological activity. Additional studies would be required to differentiate between these possibilities. In any event, the current results demonstrate that significant curvature-generating activity must reside in other regions of the protein, which likely include the transmembrane domains. In this regard, the tubule substructure we document here is consistent with a 3D model of P/rds that estimates an ~6-nm diameter for the transmembrane domains of the tetrameric protein (13). Our observations suggest that linear arrays of tetramers may pack closely together to shape the high-curvature tubules (and potentially photoreceptor disk rims).

Interestingly, P/rds-associated high-curvature tubules are present in the rod photoreceptors of rhodopsin knock-out mice. These cells cannot elaborate OSs, and instead generate rudiments filled with P/rds-containing membranes with tubular and vesicular profiles (61). A recent 3D TEM-tomography study has resolved these structures as high-curvature tubules derived from the ciliary plasma membrane.[3] Thus, the machinery responsible for OS disk morphogenesis appears limited to producing high-curvature P/rds-enriched tubules when inadequate rhodopsin is available to synthesize normal disks.

The striking tubulovesicular structures generated by P/rdsΔAH are significant for several reasons. First, the robust activity displayed by this mutant adds weight to the currently limited evidence that P/rds functions directly as a membrane-shaping protein. Second, the fact that AH loss *promoted* membrane curvature introduces the possibility that this motif (and therefore the C-terminal domain) may play a regulatory role for P/rds function. Finally, the establishment of a robust and reproducible assay for P/rds function, which is amenable to genetic manipulation, means that the long-pursued goal of establishing rational genotype-phenotype correlations for the many pathogenic defects in this protein may finally be in sight.

Altogether, this report advances knowledge and understanding of P/rds structure and function. It implicates the P/rds C terminus as a participant in interaction with GARPs, and it demonstrates that the central portion of this domain can partition into phospholipid membranes as an AH and can specifically participate in (but is not required for) membrane curvature generation. Combined with previous studies, the current findings suggest that pathogenic mutations affecting the C terminus of human P/rds can act through one or more of several mechanisms (including altering GARP2 binding, dysregulating curvature-generating activity, and/or impairing protein targeting) and set the stage for use of engineered animal models to gain more detailed understanding of related human retinopathies.

Experimental procedures

Recombinant protein production

All DNA constructs were sequence-verified prior to use. Previously generated constructs (47), which contain the full-length coding regions of bovine WT P/rds (pcPERS) and WT Rom-1 (pcROMS), subcloned into the pcDNA3 mammalian expression vector (Invitrogen) were used for stable transformation of HEK AD293 cells. From pcPERS, we derived a construct encoding mutant P/rds, pcPdAH. A combination of polymerase chain reaction (PCR) amplification and Gibson assembly was used to delete the nucleotides encoding amino acid residues 310–325 (KSVPETWKAFLESVKK). The new construct encodes a protein, P/rdsΔAH, that lacks only the inducible C-terminal AH. The coding sequence of P/rdsΔAH was also subcloned into a vector for expression in *X. laevis* rod photoreceptors to create the pXPdAH-CG construct. This plasmid utilized a pHGCR-lox backbone (a kind gift of Dr. Daniel Buchholz), which includes flanking I-SceI sites and tandem HS4 insulator sequences. The two existing cassettes in pHGCR-lox (HSP-GFP and CMV-dsRED) were replaced with the following: 1) a

[3] S. Volland and D. S. Williams (UCLA), personal communication.

0.8-kb *Xenopus* rod opsin promoter fragment driving P/rdsΔAH expression in rod photoreceptors, and 2) a crystalline promoter fragment driving expression of GFP in the lens. Standard techniques were used to subclone these fragments; the upstream cassette was derived from pOLM2 (22) and pcPdAH (described above), and the downstream cassette was derived from pDPCrtTA-TREG (62), a kind gift of Dr. Daniel Buchholz.

Expression and purification of CTER (from GST-CTER) in *E. coli* have been described previously (18). To generate a His_6-CTER pcDNA3 construct for expression in mammalian cells, cassette mutagenesis with synthetic oligonucleotides (forward, 5′-agcttgccgccaccatgggccatcaccatcaccatcacg-3′; reverse, 5′-gatccgtgatggtgatggtgatggcccatggtggcggca-3′) was used to add six histidines to the CTER N terminus. A pcDNA3-based expression vector for bovine GARP2 expression in mammalian cells was constructed by subcloning the GARP2 coding region from the previously generated pcGGa plasmid (38). Expression of His_6-CTER and GARP2 proteins in HEK AD293 cells by transient transfection using FuGENE 6 (Roche Applied Science) was performed essentially as recommended by the manufacturer.

Generation and transient transfection of stable cell lines

HEK AD293 cells (a subline of HEK 293 with enhanced adhesive properties; Stratagene, Inc.) were previously validated for full-length P/rds expression using transient transfection (48). Cells were transfected with purified and linearized pcDNA3-based plasmids, using XtremeGENE 9 according to the manufacturer's protocol (Roche Applied Science). Constructs encoding bovine orthologs of WT P/rds, P/rdsΔAH, and Rom-1 were utilized. Cells were maintained in DMEM containing 10% FBS and penicillin and streptomycin for 3 days, at which time geneticin (G418) was added (1 mg/ml). After 2–3 weeks, isolated colonies were collected and individually subcultured in selective media. Subcultured cells expressing the protein of interest (as assayed by immunocytochemistry) were subjected to a second round of cloning by limiting dilution, and protein expression was confirmed by Western blotting. Selected clones were expanded, frozen, and stored in liquid nitrogen. Continued subculture of stably expressing lines was conducted in the presence of 0.7 mg/ml geneticin in DMEM supplemented with 10% FBS. Experiments were performed on cells subjected to fewer than 20 passages. Transient transfections of stably transformed HEK AD293 cells with X-tremeGENE 9 reagent were performed according to the manufacturer's specifications and essentially as described previously (47).

Protein expression and immunoprecipitation analysis in transgenic X. laevis

Transgenic *X. laevis* were generated at the National *Xenopus* Resource (Woods Hole, MA), using an I-SceI meganuclease method, essentially as described (63). Plasmid pXPdAH-CG was digested with I-SceI and injected into fertilized eggs, and viable embryos were reared at 18 °C on a 12:12 light cycle. At 5–7 days post-fertilization (dpf) and again at 10–12 dpf, tadpoles were screened for ocular lens GFP fluorescence using a Nikon Optiphot-2 microscope equipped with an epifluorescence illuminator and GFP filter set. Transgenic tadpoles (and non-transgenic controls) were sacrificed at 14–16 dpf for analysis by Tricaine overdose and pithing. Eyes were enucleated and either snap-frozen for use in biochemical analyses or were cryoprotected with 20% sucrose and frozen in Optimal Cutting Temperature (OCT) compound for immunohistochemical analyses. All samples were stored at −80 °C until use.

For immunoprecipitation experiments, the eyes from eight tadpoles were used to immunoprecipitate endogenous P/rds, followed by immunoblotting to determine whether the transgenic bovine P/rds would co-immunoprecipitate. Immunoprecipitation analyses were conducted using anti-xP/rds Mab 1G9 covalently coupled to Sepharose beads at 5 mg of purified IgG/ml of beads (CNBr-activated Sepharose 4B, GE Healthcare). Proteins from 16 tadpole eyes (eight tadpoles) were solubilized on ice (30 min) with gentle vortexing in Buffer L, containing 50 mM Tris-HCl (pH 7.5), 1% Triton X-100, and 1× protease inhibitor mixture with 1 mM EDTA (Roche Applied Science). The solution was diluted 7-fold with PBS and then centrifuged at 30,000 rpm for 30 min at 4 °C. The clarified extract was then incubated with immunoaffinity matrix (60 μl of beads) for 1 h with gentle agitation at room temperature. After collection of the unbound fraction, beads were washed with 12 volumes of 0.1% Triton X-100 in PBS, and bound proteins were eluted in Laemmli sample buffer by heating (95 °C) for 10 min. Fractions were analyzed by Western blotting using the procedures detailed above and the following primary antibodies: anti-frog P/rds and anti-bovine P/rds PabBCT. Digital densitometry was conducted using the LiCor Odyssey software.

Immunohistochemistry and immunocytochemistry

IHC analyses were performed on ocular cryosections (12 μm) from transgenic positive tadpoles, essentially as described (38). For immunocytochemical analyses, HEK AD293 (Stratagene) cells were plated in 2-well chamber slides (Lab-Tek) and processed for immunocytofluorescence analysis essentially as described (Ritter *et al.* (38)) using anti-P/rds MabC6 (Goldberg *et al.* (48)) or PabBCT (Goldberg *et al.*, (70)) in combination with the following antibodies as indicated: anti-KDEL antibody (Abcam), anti-p58 (kind gift of Dr. Jaakko Saraste), anti-giantin (Abcam), anti-Rab11 (BD Biosciences), and anti-pan-GARP (rabbit sera raised against an N-terminal synthetic peptide coupled to BSA; MLGWVQRVLPQPPGTPQKTK).

Laser scanning confocal microscopy

Subsaturated image Z-stacks were acquired with a Nikon C1 laser-scanning confocal microscope using a ×60 oil objective (1.4 N.A.), 30-μm confocal aperture, 70-nm pixel, and 0.2-μm step sizes. No adjustments (other than cropping and annotation) were made to the images. Images presented are single optical sections taken from the midpoint of a given Z-stack, unless otherwise noted. Full Z-stack volume views are provided as supplemental data. Co-localization was quantified by Pearson's correlation coefficient using the Nikon Elements software.

Analysis of CTER-membrane interactions by ITF and circular dichroism spectroscopy

CTER protein was generated as described above and was analyzed in the presence and absence of large (100 nm) unilamellar phospholipid liposomes. LUVs of three differing compositions were used for the studies. The first two compositions utilize known rod OS phospholipid headgroup distributions and cholesterol content (64, 65); we created anionic and uncharged variants. The third is a previously used composition used for equilibrium measurements of peptide and protein partitioning into membranes (66, 67). OS-like liposomes contained 1,2-dioleoyl-*sn*-glycero-3-phosphocholine (DOPC), 1,2-dioleoyl-*sn*-glycero-3-phosphoethanolamine (DOPE), 1,2-dioleoyl-*sn*-glycero-3-phosphoserine (DOPS), and cholesterol in a 5:4:1:1 molar ratio. Uncharged (neutral) OS-like liposomes contained DOPC, DOPE, and cholesterol in a 6:4:1 molar ratio. OS-like liposomes (both charged and uncharged) were generated by hydration of dried lipid films in 10 mM sodium citrate buffer, 100 mM KCl (pH 8.0), followed by manual extrusion (68) through defined pore size polycarbonate membranes (Whatman). 1-Palmitoyl-2-oleoyl-3-phosphatidylcholine (POPC)/1-palmitoyl-2-oleoyl-*sn*-glycero-3-phospho-(1′-racemic-glycerol) (sodium salt) (POPG) liposomes were prepared at 1:3 molar ratio. Lipid stocks were mixed and then dried under a high vacuum for ~12 h. The dried lipid mixtures were hydrated in 10 mM citric buffer, 100 mM KCl (pH 8.0), and 100 nm LUVs were extruded as described (69). All lipids were obtained from Avanti Polar Lipids, Inc., and were stored at −80 °C in chloroform under a nitrogen atmosphere.

Steady-state fluorescence spectroscopy was performed using a SPEX Flurolog FL 3-22 steady-state fluorescence spectrometer (Jobin Yvon, Edison, NJ) equipped with double grating excitation and emission monochromators. The measurements were made at 25 °C in 2 × 10-mm cuvettes, oriented perpendicular to the excitation beam. For tryptophan fluorescence measurements, excitation wavelengths were 280 nm and emission spectra were recorded between 290 and 500 nm, using excitation and emission spectral slits of 2 mm and 4 nm, respectively. CTER (2 μM) was mixed with LUV in 10 mM sodium citrate buffer (pH 8.0), and gradual acidification was achieved by addition of small amounts of 2.5 M acetic buffer. All spectra were recorded after 15 min of incubation to ensure the equilibrium of the sample. Correction for the background and fitting of all spectra to calculate the position of maximum emission was done as described previously (53).

Circular dichroism (CD) measurements were performed on peptides at 5 μM using an upgraded Jasco-720 spectropolarimeter (Japan Spectroscopic Co., Tokyo, Japan) at 25 °C, controlled by a Peltier unit. Normally 80–100 scans were recorded to increase the signal-to-noise ratio at 190–260 nm using a 1-mm optical path. CTER was prepared in 10 mM sodium citrate buffer, 100 mM KCl (pH 8.0), and LUVs were added to a final phospholipid concentration of 1 mM. Samples were allowed to equilibrate with mixing for 15 min before spectra were collected. Adjustments of pH were achieved by addition of 2.5 M acetic acid buffer. Spectra were corrected for background scattering by subtracting LUV-only spectra.

HEK AD293 cell ultrastructure and immunogold protein localization

HEK AD293 cells cultured in 100-mm dishes were processed in 0.1 M Sorensen's buffer (pH 7.4), at room temperature for embedding in Polybed 812 (Electron Microscopy Sciences). Cells were fixed for 1.5 h in 2.5% glutaraldehyde, osmicated for 15 min in 1% osmium tetroxide, and stained *en bloc* in 2% aqueous uranyl acetate for 10 min. Following EtOH dehydration, cells were infiltrated serially with EtOH/Polybed 812 (3:1), EtOH/Polybed 812 (1:1), EtOH/Polybed 812 (1:3), and pure Polybed 812. Cells were then scraped from plates and pelleted in Beem capsules by centrifugation, and the resin was polymerized at 60 °C for 24 h. Thin sections were mounted on copper grids and post-stained with uranyl acetate and lead citrate.

For post-embedding immunogold labeling in LR White resin (Electron Microscopy Sciences), HEK AD293 cells cultured in 100-mm dishes were fixed 1.5 h in 4% paraformaldehyde, 0.5% glutaraldehyde, in 0.1 M Sorensen's buffer, (pH 7.4), at room temperature. Following fixation, cells were incubated for 1 h in 1% tannic acid and stained *en bloc* 20 min in 2% aqueous uranyl acetate. Cells were subjected to graded EtOH dehydration and infiltrated with EtOH/LR White (1:1) and then pure LR White. Cells were scraped from plates and pelleted in Beem capsules by centrifugation, and the resin was polymerized at 50 °C for 48 h or under UV illumination at 10 °C for 24 h. Thin sections were mounted on Formvar/carbon-coated grids and were processed with anti-P/rds Mab2B6 (a kind gift of Dr. Robert S. Molday) in the presence (1000-fold molar excess) or absence of a peptide corresponding to the antibody epitope. Secondary antibody labeling was performed with a 1:50 dilution of goat anti-mouse 1.4-nm gold-conjugated IgG (Nanoprobes; Yaphank, NY), which was enhanced with HQ Silver (Nanoprobes, Inc.). Sections were post-stained with 0.1% aqueous osmium tetroxide, followed by uranyl acetate and lead citrate.

TEM imaging was performed using a FEI Morgagni instrument at 80 kV, using a side-mount Hamamatsu Orca-HR digital camera and AMT Image Capture Engine Version 601 software and size-calibrated using a grating replica (Electron Microscopy Sciences). Brightness and contrast of some images were adjusted to facilitate comparisons. Analyses of tubule diameter in tubulovesicular membrane inclusions were performed using the ImageJ software (National Institutes of Health) line tool. Three cells possessing tubulovesicular network inclusions were selected at random from a post-stained section. Tubule outer diameters were measured with a line drawn perpendicular to the tubule axis, at points where tubule diameters remained constant for at least 50 nm. All distinct tubules within each selected cell were counted (at least 50–100 measurements/cell). Analyses of tubulovesicular inclusion frequency (proportion of cells having at least one inclusion) and extent (inclusion area) were conducted by a blinded observer on 60–90 randomly selected cells from three independent transfections. The cytoplasm of each cell was inspected at 22,000–44,000× direct magnification for the presence/absence of tubulovesicular inclusions, using criteria of at least three clearly resolvable trifurcated cisternae with small diameter (≤40 nm) and uniform branches, in close proximity to multiple (>5) small diameter (≤40 nm)

tubules possessing electron dense acini. Quantification of tubulovesicular membrane inclusion areas was performed using the ImageJ software (National Institutes of Health) polygon tool; areas summed over the population assayed were normalized to the number of cells in that population.

Author contributions—M. L. M. designed, performed, and analyzed the experiments shown in Figs. 4 and 7. V. A. K. performed and analyzed the experiments shown in Figs. 8 and 9. C. G. designed, performed, and analyzed the experiments shown in Fig. 6. A. F. X. G. designed, performed, and analyzed the experiments shown in Figs. 2, 3, and 5. M. L. M., V. A. K., A. S. L., and A. F. X. G. interpreted results, generated the figures, and wrote/edited the manuscript.

Acknowledgments—We thank Linda Ritter for design and generation of DNA constructs and for the generation and initial characterization of the stable HEK AD293 cell lines; Dr. Daniel Buchholz for pHGCR-lox and pDPCrtTA-TREG plasmids; Dr. Robert Molday for the Mab2B6 antibody; Dr. Jaakko Saraste for the anti-p58/ERGIC antibody; Victor Montes and Breyanna Cavanaugh for assistance with figure preparation; and Beatrice Tam for helpful discussions.

References

1. Kennedy, B., and Malicki, J. (2009) What drives cell morphogenesis: a look inside the vertebrate photoreceptor. *Dev. Dyn.* **238,** 2115–2138
2. Wensel, T. G. (2008) Signal transducing membrane complexes of photoreceptor outer segments. *Vision Res.* **48,** 2052–2061
3. Young, R. W. (1976) Visual cells and the concept of renewal. *Invest. Ophthalmol. Vis. Sci.* **15,** 700–725
4. Wensel, T. G., Zhang, Z., Anastassov, I. A., Gilliam, J. C., He, F., Schmid, M. F., and Robichaux, M. A. (2016) Structural and molecular bases of rod photoreceptor morphogenesis and disease. *Prog. Retin. Eye Res.* **55,** 32–51
5. Veleri, S., Lazar, C. H., Chang, B., Sieving, P. A., Banin, E., and Swaroop, A. (2015) Biology and therapy of inherited retinal degenerative disease: insights from mouse models. *Dis. Model. Mech.* **8,** 109–129
6. Goldberg, A. F., Moritz, O. L., and Williams, D. S. (2016) Molecular basis for photoreceptor outer segment architecture. *Prog. Retin. Eye Res.* **55,** 52–81
7. Falk, G., and Fatt, P. (1973) Changes in structure of the disks of retinal rods in hypotonic solutions. *J. Cell Sci.* **13,** 787–797
8. Falk, G., and Fatt, P. (1969) Distinctive properties of the lamellar and disk-edge structures of the rod outer segment. *J. Ultrastruct. Res.* **28,** 41–60
9. Molday, R. S., and Moritz, O. L. (2015) Photoreceptors at a glance. *J. Cell Sci.* **128,** 4039–4045
10. Steinberg, R. H., Fisher, S. K., and Anderson, D. H. (1980) Disc morphogenesis in vertebrate photoreceptors. *J. Comp. Neurol.* **190,** 501–508
11. Anderson, D. H., Fisher, S. K., and Steinberg, R. H. (1978) Mammalian cones: disc shedding, phagocytosis, and renewal. *Invest. Ophthalmol. Vis. Sci.* **17,** 117–133
12. Shibata, Y., Hu, J., Kozlov, M. M., and Rapoport, T. A. (2009) Mechanisms shaping the membranes of cellular organelles. *Annu. Rev. Cell Dev. Biol.* **25,** 329–354
13. Kevany, B. M., Tsybovsky, Y., Campuzano, I. D., Schnier, P. D., Engel, A., and Palczewski, K. (2013) Structural and functional analysis of the native peripherin-ROM1 complex isolated from photoreceptor cells. *J. Biol. Chem.* **288,** 36272–36284
14. Khattree, N., Ritter, L. M., and Goldberg, A. F. (2013) Membrane curvature generation by a C-terminal amphipathic helix in peripherin-2/rds, a tetraspanin required for photoreceptor sensory cilium morphogenesis. *J. Cell Sci.* **126,** 4659–4670
15. Molday, R. S., Hicks, D., and Molday, L. (1987) Peripherin. A rim-specific membrane protein of rod outer segment discs. *Invest. Ophthalmol. Vis. Sci.* **28,** 50–61
16. Travis, G. H., Groshan, K. R., Lloyd, M., and Bok, D. (1992) Complete rescue of photoreceptor dysplasia and degeneration in transgenic retinal degeneration slow (*rds*) mice. *Neuron* **9,** 113–119
17. Stuck, M. W., Conley, S. M., and Naash, M. I. (2016) PRPH2/RDS and ROM-1: historical context, current views and future considerations. *Prog. Retin. Eye Res.* **52,** 47–63
18. Ritter, L. M., Arakawa, T., and Goldberg, A. F. (2005) Predicted and measured disorder in peripherin/rds, a retinal tetraspanin. *Protein Pept. Lett.* **12,** 677–686
19. Wright, P. E., and Dyson, H. J. (2015) Intrinsically disordered proteins in cellular signalling and regulation. *Nat. Rev. Mol. Cell Biol.* **16,** 18–29
20. Boesze-Battaglia, K., Goldberg, A. F., Dispoto, J., Katragadda, M., Cesarone, G., and Albert, A. D. (2003) A soluble peripherin/Rds C-terminal polypeptide promotes membrane fusion and changes conformation upon membrane association. *Exp. Eye Res.* **77,** 505–514
21. Edrington, T. C., 5th., Lapointe, R., Yeagle, P. L., Gretzula, C. L., and Boesze-Battaglia, K. (2007) Peripherin-2: an intracellular analogy to viral fusion proteins. *Biochemistry* **46,** 3605–3613
22. Tam, B. M., Moritz, O. L., and Papermaster, D. S. (2004) The C terminus of peripherin/rds participates in rod outer segment targeting and alignment of disk incisures. *Mol. Biol. Cell* **15,** 2027–2037
23. Salinas, R. Y., Baker, S. A., Gospe, S. M., 3rd., and Arshavsky, V. Y. (2013) A single valine residue plays an essential role in peripherin/rds targeting to photoreceptor outer segments. *PLoS ONE* **8,** e54292
24. Tian, G., Ropelewski, P., Nemet, I., Lee, R., Lodowski, K. H., and Imanishi, Y. (2014) An unconventional secretory pathway mediates the cilia targeting of peripherin/rds. *J. Neurosci.* **34,** 992–1006
25. Boon, C. J., den Hollander, A. I., Hoyng, C. B., Cremers, F. P., Klevering, B. J., and Keunen, J. E. (2008) The spectrum of retinal dystrophies caused by mutations in the peripherin/RDS gene. *Prog. Retin. Eye Res.* **27,** 213–235
26. Goldberg, A. F., and Molday, R. S. (2000) Expression and characterization of peripherin/rds-Rom-1 complexes and mutants implicated in retinal degenerative diseases. *Methods Enzymol.* **316,** 671–687
27. Goldberg, A. F., Moritz, O. L., and Molday, R. S. (1995) Heterologous expression of photoreceptor peripherin/rds and Rom-1 in COS-1 cells: assembly, interactions, and localization of multisubunit complexes. *Biochemistry* **34,** 14213–14219
28. Stuck, M. W., Conley, S. M., and Naash, M. I. (2015) Retinal degeneration slow (RDS) glycosylation plays a role in cone function and in the regulation of RDS.ROM-1 protein complex formation. *J. Biol. Chem.* **290,** 27901–27913
29. Goldberg, A. F., Loewen, C. J., and Molday, R. S. (1998) Cysteine residues of photoreceptor peripherin/rds: role in subunit assembly and autosomal dominant retinitis pigmentosa. *Biochemistry* **37,** 680–685
30. Loewen, C. J., and Molday, R. S. (2000) Disulfide-mediated oligomerization of Peripherin/Rds and Rom-1 in photoreceptor disk membranes. Implications for photoreceptor outer segment morphogenesis and degeneration. *J. Biol. Chem.* **275,** 5370–5378
31. Goldberg, A. F., and Molday, R. S. (1996) Subunit composition of the peripherin/rds-rom-1 disk rim complex from rod photoreceptors: hydrodynamic evidence for a tetrameric quaternary structure. *Biochemistry* **35,** 6144–6149
32. Goldberg, A. F., and Molday, R. S. (1996) Defective subunit assembly underlies a digenic form of retinitis pigmentosa linked to mutations in peripherin/rds and rom-1. *Proc. Natl. Acad. Sci. U.S.A.* **93,** 13726–13730
33. Kedzierski, W., Nusinowitz, S., Birch, D., Clarke, G., McInnes, R. R., Bok, D., and Travis, G. H. (2001) Deficiency of rds/peripherin causes photoreceptor death in mouse models of digenic and dominant retinitis pigmentosa. *Proc. Natl. Acad. Sci. U.S.A.* **98,** 7718–7723
34. Clarke, G., Goldberg, A. F., Vidgen, D., Collins, L., Ploder, L., Schwarz, L., Molday, L. L., Rossant, J., Szél, A., Molday, R. S., Birch, D. G., and McInnes, R. R. (2000) Rom-1 is required for rod photoreceptor viability and the regulation of disk morphogenesis. *Nat. Genet.* **25,** 67–73
35. Ding, X. Q., Nour, M., Ritter, L. M., Goldberg, A. F., Fliesler, S. J., and Naash, M. I. (2004) The R172W mutation in peripherin/rds causes a cone-rod dystrophy in transgenic mice. *Hum. Mol. Genet.* **13,** 2075–2087

36. Loewen, C. J., Moritz, O. L., Tam, B. M., Papermaster, D. S., and Molday, R. S. (2003) The role of subunit assembly in peripherin-2 targeting to rod photoreceptor disk membranes and retinitis pigmentosa. *Mol. Biol. Cell* **14,** 3400–3413
37. Tam, B. M., Lai, C. C., Zong, Z., and Moritz, O. L. (2013) Generation of transgenic *X. laevis* models of retinal degeneration. *Methods Mol. Biol.* **935,** 113–125
38. Ritter, L. M., Khattree, N., Tam, B., Moritz, O. L., Schmitz, F., and Goldberg, A. F. (2011) *In situ* visualization of protein interactions in sensory neurons: glutamic acid-rich proteins (GARPs) play differential roles for photoreceptor outer segment scaffolding. *J. Neurosci.* **31,** 11231–11243
39. Poetsch, A., Molday, L. L., and Molday, R. S. (2001) The cGMP-gated channel and related glutamic acid-rich proteins interact with peripherin-2 at the rim region of rod photoreceptor disc membranes. *J. Biol. Chem.* **276,** 48009–48016
40. Colville, C. A., and Molday, R. S. (1996) Primary structure and expression of the human β-subunit and related proteins of the rod photoreceptor cGMP-gated channel. *J. Biol. Chem.* **271,** 32968–32974
41. Snider, C., Jayasinghe, S., Hristova, K., and White, S. H. (2009) MPEx: a tool for exploring membrane proteins. *Protein Sci.* **18,** 2624–2628
42. Teixeira, V. H., Vila-Viçosa, D., Reis, P. B., and Machuqueiro, M. (2016) pK(a) values of titrable amino acids at the water/membrane interface. *J. Chem. Theory Comput.* **12,** 930–934
43. Vargas-Uribe, M., Rodnin, M. V., and Ladokhin, A. S. (2013) Comparison of membrane insertion pathways of the apoptotic regulator Bcl-xL and the diphtheria toxin translocation domain. *Biochemistry* **52,** 7901–7909
44. Kyrychenko, A., Vasquez-Montes, V., Ulmschneider, M. B., and Ladokhin, A. S. (2015) Lipid headgroups modulate membrane insertion of pHLIP peptide. *Biophys. J.* **108,** 791–794
45. Hu, J., Shibata, Y., Voss, C., Shemesh, T., Li, Z., Coughlin, M., Kozlov, M. M., Rapoport, T. A., and Prinz, W. A. (2008) Membrane proteins of the endoplasmic reticulum induce high-curvature tubules. *Science* **319,** 1247–1250
46. Drin, G., and Antonny, B. (2010) Amphipathic helices and membrane curvature. *FEBS Lett.* **584,** 1840–1847
47. Ritter, L. M., Boesze-Battaglia, K., Tam, B. M., Moritz, O. L., Khattree, N., Chen, S. C., and Goldberg, A. F. (2004) Uncoupling of photoreceptor peripherin/rds fusogenic activity from biosynthesis, subunit assembly, and targeting: a potential mechanism for pathogenic effects. *J. Biol. Chem.* **279,** 39958–39967
48. Goldberg, A. F., Fales, L. M., Hurley, J. B., and Khattree, N. (2001) Folding and subunit assembly of photoreceptor peripherin/rds is mediated by determinants within the extracellular/intradiskal EC2 domain: implications for heterogeneous molecular pathologies. *J. Biol. Chem.* **276,** 42700–42706
49. Zhang, Y., Molday, L. L., Molday, R. S., Sarfare, S. S., Woodruff, M. L., Fain, G. L., Kraft, T. W., and Pittler, S. J. (2009) Knockout of GARPs and the β-subunit of the rod cGMP-gated channel disrupts disk morphogenesis and rod outer segment structural integrity. *J. Cell Sci.* **122,** 1192–1200
50. Hüttl, S., Michalakis, S., Seeliger, M., Luo, D. G., Acar, N., Geiger, H., Hudl, K., Mader, R., Haverkamp, S., Moser, M., Pfeifer, A., Gerstner, A., Yau, K. W., and Biel, M. (2005) Impaired channel targeting and retinal degeneration in mice lacking the cyclic nucleotide-gated channel subunit CNGB1. *J. Neurosci.* **25,** 130–138
51. Batra-Safferling, R., Abarca-Heidemann, K., Körschen, H. G., Tziatzios, C., Stoldt, M., Budyak, I., Willbold, D., Schwalbe, H., Klein-Seetharaman, J., and Kaupp, U. B. (2006) Glutamic acid-rich proteins of rod photoreceptors are natively unfolded. *J. Biol. Chem.* **281,** 1449–1460
52. Boesze-Battaglia, K., Stefano, F. P., Fenner, M., and Napoli, A. A., Jr. (2000) A peptide analogue to a fusion domain within photoreceptor peripherin/rds promotes membrane adhesion and depolarization. *Biochim. Biophys. Acta* **1463,** 343–354
53. Ladokhin, A. S., Jayasinghe, S., and White, S. H. (2000) How to measure and analyze tryptophan fluorescence in membranes properly, and why bother? *Anal. Biochem.* **285,** 235–245
54. Ladokhin, A. S., Fernández-Vidal, M., and White, S. H. (2010) CD spectroscopy of peptides and proteins bound to large unilamellar vesicles. *J. Membr. Biol.* **236,** 247–253
55. Chen, C., Jiang, Y., and Koutalos, Y. (2002) Dynamic behavior of rod photoreceptor disks. *Biophys. J.* **83,** 1403–1412
56. Westrate, L. M., Lee, J. E., Prinz, W. A., and Voeltz, G. K. (2015) Form follows function: the importance of endoplasmic reticulum shape. *Annu. Rev. Biochem.* **84,** 791–811
57. Zurek, N., Sparks, L., and Voeltz, G. (2011) Reticulon short hairpin transmembrane domains are used to shape ER tubules. *Traffic* **12,** 28–41
58. Shibata, Y., Voss, C., Rist, J. M., Hu, J., Rapoport, T. A., Prinz, W. A., and Voeltz, G. K. (2008) The reticulon and DP1/Yop1p proteins form immobile oligomers in the tubular endoplasmic reticulum. *J. Biol. Chem.* **283,** 18892–18904
59. Simunovic, M., Evergren, E., Golushko, I., Prévost, C., Renard, H. F., Johannes, L., McMahon, H. T., Lorman, V., Voth, G. A., and Bassereau, P. (2016) How curvature-generating proteins build scaffolds on membrane nanotubes. *Proc. Natl. Acad. Sci.* **113,** 11226–11231
60. Chen, Z., Zhu, C., Kuo, C. J., Robustelli, J., and Baumgart, T. (2016) The N-terminal amphipathic helix of endophilin does not contribute to its molecular curvature generation capacity. *J. Am. Chem. Soc.* **138,** 14616–14622
61. Lee, E. S., Burnside, B., and Flannery, J. G. (2006) Characterization of peripherin/rds and rom-1 transport in rod photoreceptors of transgenic and knockout animals. *Invest. Ophthalmol. Vis. Sci.* **47,** 2150–2160
62. Choi, J., Moskalik, C. L., Ng, A., Matter, S. F., and Buchholz, D. R. (2015) Regulation of thyroid hormone-induced development *in vivo* by thyroid hormone transporters and cytosolic binding proteins. *Gen. Comp. Endocrinol.* **222,** 69–80
63. Ogino, H., McConnell, W. B., and Grainger, R. M. (2006) High-throughput transgenesis in *Xenopus* using I-SceI meganuclease. *Nat. Protoc.* **1,** 1703–1710
64. Anderson, R. E., and Maude, M. B. (1970) Phospholipids of bovine outer segments. *Biochemistry* **9,** 3624–3628
65. Fliesler, S. J., and Schroepfer, G. J., Jr. (1982) Sterol composition of bovine retinal rod outer segment membranes and whole retinas. *Biochim. Biophys. Acta* **711,** 138–148
66. Posokhov, Y. O., Gottlieb, P. A., Morales, M. J., Sachs, F., and Ladokhin, A. S. (2007) Is lipid bilayer binding a common property of inhibitor cysteine knot ion-channel blockers? *Biophys. J.* **93,** L20-L22
67. Vargas-Uribe, M., Rodnin, M. V., Öjemalm, K., Holgado, A., Kyrychenko, A., Nilsson, I., Posokhov, Y. O., Makhatadze, G., von Heijne, G., and Ladokhin, A. S. (2015) Thermodynamics of membrane insertion and refolding of the diphtheria toxin T-domain. *J. Membr. Biol.* **248,** 383–394
68. MacDonald, R. C., MacDonald, R. I., Menco, B. P., Takeshita, K., Subbarao, N. K., and Hu, L. R. (1991) Small-volume extrusion apparatus for preparation of large, unilamellar vesicles. *Biochim. Biophys. Acta* **1061,** 297–303
69. Hope, M. J., Bally, M. B., Mayer, L. D., Janoff, A. S., and Cullis, P. R. (1986) Generation of multilamellar and unilamellar phospholipid vesicles. *Chem. Phys. Lipids* **40,** 89–107
70. Goldberg, A. F. X., Ritter, L. M., Khattree, N., Peachey, N. S., Fariss, R. N., Dang, L., Yu, M., and Bottrell, A. R. (2007) An intramembrane glutamic acid governs peripherin/rds function for photoreceptor disk morphogenesis. *Invest. Ophthalmol. Vis. Sci.* **48,** 2975–2986